Check for updates

Received: 5 June 2022 | Revised: 4 August 2022 | Accepted: 2 September 2022

DOI: 10.1002/nme.7121

RESEARCH ARTICLE

WILEY

Cellular topology optimization on differentiable Voronoi diagrams

Fan Feng[1] | **Shiying Xiong**[1] | **Ziyue Liu**[1] | **Zangyueyang Xian**[1] | **Yuqing Zhou**[2] | **Hiroki Kobayashi**[3] | **Atsushi Kawamoto**[3] | **Tsuyoshi Nomura**[3] | **Bo Zhu**[1]

[1]Computer Science Department, Dartmouth College, Hanover, New Hampshire, USA

[2]Toyota Research Institute of North America, Ann Arbor, Michigan, USA

[3]Toyota Central R & D Labs, Nagakute, Japan

Correspondence
Tsuyoshi Nomura, Koraku Mori Building 10F, 1 - 4 - 14 Koraku, Bunkyo-ku, Tokyo 112-0004, Japan
Email: nomu2@mosk.tytlabs.co.jp
Bo Zhu, Computer Science Department, Dartmouth College, New Hampshire, USA.
Email: bo.zhu@dartmouth.edu

Abstract

Cellular structures manifest their outstanding mechanical properties in many biological systems. One key challenge for designing and optimizing these geometrically complicated structures lies in devising an effective geometric representation to characterize the system's spatially varying cellular evolution driven by objective sensitivities. A conventional discrete cellular structure, for example, a Voronoi diagram, whose representation relies on discrete Voronoi cells and faces, lacks its differentiability to facilitate large-scale, gradient-based topology optimizations. We propose a topology optimization algorithm based on a differentiable and generalized Voronoi representation that can evolve the cellular structure as a continuous field. The central piece of our method is a hybrid particle-grid representation to encode the previously discrete Voronoi diagram into a continuous density field defined in a Euclidean space. Based on this differentiable representation, we further extend it to tackle anisotropic cells, free boundaries, and functionally-graded cellular structures. Our differentiable Voronoi diagram enables the integration of an effective cellular representation into the state-of-the-art topology optimization pipelines, which defines a novel design space for cellular structures to explore design options effectively that were impractical for previous approaches. We showcase the efficacy of our approach by optimizing cellular structures with up to thousands of anisotropic cells, including femur bone and Odonata wing.

KEYWORDS

cellular structure, differentiable Voronoi diagram, topology optimization

1 | INTRODUCTION

Cellular and foam structures are ubiquitous in nature. Examples range from honeycombs,[1] bone interiors,[2] insect wings,[3] to foam bubbles,[4] all of which exhibit a wide range of material properties and functionalities that cannot be realized with traditional engineering configurations. Developing mechanistic understanding and numerical optimization of cellular structures with complex geometric patterns have received extensive attention in both scientific and engineering communities.[5] For example, experiments, simulations, and data analysis have been carried out to study the insect wing morphology,[6] leaf vein topology,[7] and sponge cake formation,[8] for the sake of uncovering the structural principles and developmental mechanics underpinning these biological systems. However, most of the existing studies and cellular

 © 2022 John Wiley & Sons, Ltd.

structural designs are based on trial-and-error experiments,[9] stochastic sampling,[10,11] and procedural methods,[12,13] which heavily relied on the materials' homogenized properties and human engineers' prior expertise. First-principle methods guided by mathematically rigorous sensitivities and numerically efficient optimization frameworks have remained an unexplored field due to three interleaving challenges in tackling cellular structures' differentiation, generalization, and discretization.

First, devising a differentiable representation for complex cellular structures is challenging. To the best of our knowledge, no current numerical approach can differentiate and optimize the topological evolution of a complex cellular structure on a single-cell level, that is, to *co-optimize the size, shape, and topology* of each local cell nested in the design domain by following continuous sensitivities of a specific design objective. Traditional cellular representations, with Voronoi diagrams[14] as a particular example, represent the geometry and topology of a cellular pattern on a discrete mesh. By defining a distance field based on a set of site points and extracting the level set with an equal distance to the two closest points, a Voronoi diagram partitions a domain into a set of discrete cells, with each cell represented by a set of faces, which are borders between incident cells, and vertices, which are intersections of incident faces. On the simulation side, numerical solvers discretized on a Voronoi diagram, or its many variations (e.g., Power diagrams[15]), have been used widely to facilitate adaptive simulations of large-scale fluid,[16,17] solid,[18] and cosmology[19] systems in scientific computing. On the geometry processing side, discrete mesh generation algorithms for Voronoi diagrams, or its dual, Delauney tessellations, have been integrated into the state-of-the-art computational geometry libraries (e.g., CGAL[20]) to render support for various computational geometry applications. Recently, a new line of efforts has been devoted to developing parallel algorithms to generate large-scale Voronoi diagrams on modern GPUs.[21,22] Despite the rapid advent of forward simulation and mesh generation, inverse procedures to differentiate a Voronoi diagram, that is, to calculate the sensitivity of a Voronoi diagram's geometric shape and topological pattern with respect to its design variables, which are essential to accommodate the various structural design and optimization applications, has remained unexplored. In the state of the art, most of the computational design of Voronoi structures in a specific physical context relies on non-gradient or procedural algorithms for the design parameter exploration. Instances include,[23] which optimizes the Voronoi structure by distributing the site points heuristically according to the structure's stress,[24] which initializes Voronoi site points inside high-density boundaries according to standard topology optimization results, and Reference 25, which iteratively deleting and adding site points to obtain a desired stress distribution on the surface. None of the above methods optimizes a Voronoi structure based on continuous sensitivity analysis. An algorithmic strategy to probe the optimal solution, by structuring the design space or enforcing strong heuristics, becomes an imperative necessity to establish an effective numerical optimization paradigm for cellular structures.

The second challenge for cellular structural optimization lies in the representation's generalizability. Most of the cellular patterns in nature do not rigorously satisfy the Voronoi definition. The cellular elements on these materials are *geometrically anisotropic*, *spatially adaptive*, and *with a free boundary*. First, cellular structures in nature are usually anisotropic, unlike a traditional Voronoi diagram whose cells exhibit a uniform distance metric in all directions. For example, the vein network of an insect wing partitions a thin shell into regions featured by a broad range of aspect ratios, encompassing cells that are small, large, thin, or slender.[26] It has also been shown in the literature that anisotropic cellular structures can lead to lower structural compliance than isotropic ones.[27] Representing an ensemble of anisotropic cellular features within a unified numerical framework requires an expressive geometric data representation that can characterize cellular patterns beyond a standard Voronoi diagram. Second, spatial adaptivity is essential for a cellular structure to obtain outstanding mechanical performance. The centroidal Voronoi tessellation (CVT) method,[28] along with other functionally-graded lattice structures,[12,29] was invented to control the spatial distribution of Voronoi cells. Wu et al.[30] utilized local volume constraints to design infill structures on a full scale, which formed uniform lattice structures. Non-uniform local volume constraints have been later proposed to design heterogeneous lattice structures.[31,32] Lastly, numerous cellular structures in nature form circular boundaries by themselves. But the regular Voronoi partition spans the entire domain. Other cellular-related representations such as the open-cell porous structure have also been investigated.[33,34] However, there is no existing work that enables the representation of cellular structure with free boundaries.

Third, it is challenging to devise an efficient numerical discretization to support the cellular structure simulation and optimization. The existing discrete data structures underpinning topology optimization applications are composed mainly of grids, particles/meshes, and their hybrid. The lattice grid is the most popular data structure empowering the density-based topology optimization.[35] However, this approach requires a very high grid resolution and well-designed filters to emerge local fine features.[36,37] Homogenization-based topology optimization plus an additional dehomogenization-based post-processing step have been applied to design cellular structures in a multi-scale way.[38-40] The resulting optimized designs, however, are considered near-optimal due to the reconstruction errors from

dehomogenization. It is noted that a similar framework has also been applied to the optimal design of microreactors with space-filling microchannel flow fields.[41] By simultaneously optimizing micro-structural cell geometries and their distributions on the macro scale, concurrent two-scale topology optimization can be used to design lattice structures.[42-44] Besides grid-based methods, Lagrangian representations, manifesting mainly as meshless particles[45] and simplicial meshes,[46] play an important role in algorithms that co-optimize a target structure's shape and topology. In these approaches, the simulation is discretized directly on a mesh or particles, and the optimization is enabled by moving the mesh vertices or meshless points in the design domain according to their sensitivities. The remeshing overhead, including repairing the simplicial mesh or redistributing particles, is one of the main bottlenecks of these approaches. None of the existing Lagrangian methods can handle the optimization of complex cellular structures. In addition to grid-based and particle-based approaches, hybrid schemes were also explored extensively in topology optimization. For instance, the moving morphing component method (MMC)[47,48] and the geometric projection method[49,50] optimize the geometric parameters (e.g., position and orientation) of a set of moving primitives that characterize the structure by projecting the union of these components on a background grid. Similar ideas can be seen in Li et al.,[45] which utilizes the communication between fixed material-point quadratures and moving particles to achieve a sub-cell representation for complex structures. Motivated by these approaches, we propose a hybrid grid-particle representation to encode the cellular pattern. Our approach distinguishes itself from the previous ones by co-optimizing the particles' positions and their local distance metric to describe the local cellular geometry, which enabled our method to evolve complicated structures without relying on abundant point samples or prohibitively high-resolution grid.

To address the aforementioned three challenges, we propose a computational approach that can differentiate, generalize, and explore the design space of complex cellular structures. We first formulate a differentiable Voronoi representation, inspired by the soft Voronoi representation in the recent computer vision literature,[51] where they devise a differentiable Voronoi diagram and embed it into a generative deep network for solid geometry representation. Akin to their method, we leverage a softmax function to partition the Voronoi regions in a differentiable fashion. We further devised a novel filter to extract the density-based Voronoi faces, which are essential for structural optimization, and devise a differentiable scheme to evolve their topology with respect to the design variables. Next, we developed a generalized Voronoi representation for anisotropic, spatially adaptive, and free-boundary-enabled cellular structures. By adopting Mahalanobis metric tensor[52] on each Voronoi site point, our method enables a heterogeneous and anisotropic Voronoi tessellation. By letting each point carry its own metric tensor, the anisotropy of the Voronoi cells can vary vigorously over the design space. These localized metric tensors, in conjunction with the moving particles, enable a spatially adaptive and anisotropic representation of cellular patterns, which greatly extend the design space of the original Voronoi diagram. To represent structures with a free boundary, we further modify our representation to support a foamy boundary, which enhances the traditional Voronoi diagram which functions primarily as a spatial partition. Last, with the hybrid grid-particle discretization, our method incorporates the differentiable Voronoi representation into the conventional solid isotropic material with penalization method (SIMP) topology-optimization framework. Furthermore, we implement a k-nearest neighbor search method to localize the computation of the differentiable Voronoi diagram to reduce the computational cost of the Voronoi diagram from $O(N^2)$ to $O(k \log N)$.

The rest of the article is organized as follows. We discuss the mathematical formulation of the differentiable, anisotropic, and spatially adaptive Voronoi partition with a free boundary in Section 2. We then integrate the Voronoi formulation into the density-based topology optimization framework in Section 3. The overall algorithm workflow and optimization are presented in Section 4. Section 5 presents extensive numerical results before conclusions are drawn in Section 6.

2 | DIFFERENTIABLE VORONOI DIAGRAM

In this section, we will formulate the mathematical definition for our differentiable, anisotropic, and spatially adaptive Voronoi representation with free boundary and its sensitivity analysis.

2.1 | Differentiable Voronoi diagram

Given a set of site points $P = \{\boldsymbol{x}_m \mid m = 1, 2, \ldots, N^c\}$ in N^d dimensional domain Ω, a Voronoi diagram is a partition of Ω into N^c polygonal regions, called Voronoi cells, with each Voronoi cell V_m associated with a site point $\boldsymbol{x}_m$. Each Voronoi

cell manifests a geometric property that $\boldsymbol{x}_m$ is the closest of the given points to any $\boldsymbol{x} \in V_m$.[53] In other words, if $\mathrm{d}_m(\boldsymbol{x}, \boldsymbol{x}_m)$ denotes the norm between the points $\boldsymbol{x}$ and $\boldsymbol{x}_m$, then

$$V_m = \{\boldsymbol{x} \in \Omega \mid \mathrm{d}_m(\boldsymbol{x}, \boldsymbol{x}_m) \leq \mathrm{d}_n(\boldsymbol{x}, \boldsymbol{x}_n) \ \text{ for all } \ n = 1, 2, \ \dots \ , N^c\}. \tag{1}$$

We remark that the norm d_m can take different forms. If d_m is a Euclidean norm, all Voronoi cells are bounded by some straight segments; otherwise, the boundary of some Voronoi cells may be curved segments (non-Euclidean norms will be discussed in Section 2.2). Based on the Euclidean norm, we show in Figure 1A the partition of a two-dimensional domain into two Voronoi cells.

To enable a differentiable partition, we introduce a modified Voronoi partition based on the softmax function[54] as follows:

$$S_m(\boldsymbol{x}) = f_m^{N^c}\left[e^{-\mathrm{d}_1(\boldsymbol{x}, \boldsymbol{x}_1)}, \ \dots \ , e^{-\mathrm{d}_{N^c}(\boldsymbol{x}, \boldsymbol{x}_{N^c})}\right], \quad m \in I_v, \tag{2}$$

where $f_m^{N^c}$ is a fractional equation

$$f_m^{N^c}(x_1, \ \dots \ , x_{N^c}) = \frac{x_m}{\sum_{n \in I_v} x_n}, \tag{3}$$

and I_v is an index set with

$$I_v \equiv \{1, \ \dots \ , N^c\}. \tag{4}$$

The softmax function is originated from physics and statistical mechanics, which recently has also been widely used as an activation function in modern neural networks.[55] The softmax function selects one item from a group by following some distance metric in a "soft" (and therefore differentiable) manner. In other words, we can build a program without an "if" statement to calculate the 0–1 density distribution that specifies the region of a given Voronoi point. Figure 1B shows the Voronoi partition formed by the softmax function, where the gray region has value one and the red region has value zero to indicate the coverage of the lower point.

In our modified Voronoi partition, we calculate the density distribution for a specific site point in Ω as

$$\rho(\boldsymbol{x}) = 1 - \sum_{m \in I_v} [S_m(\boldsymbol{x})]^{\beta}, \tag{5}$$

where β controls the sharpness of the edge as illustrated in Figure 2. As shown in Figure 2A, when $\beta = 1$, no edge will appear since the soft max values are simply added together. Comparing Figure 2B,C, we can see there is a positive correlation between the value of β and the sharpness of the edges. It is noticeable that as β increases, the thickness of edges

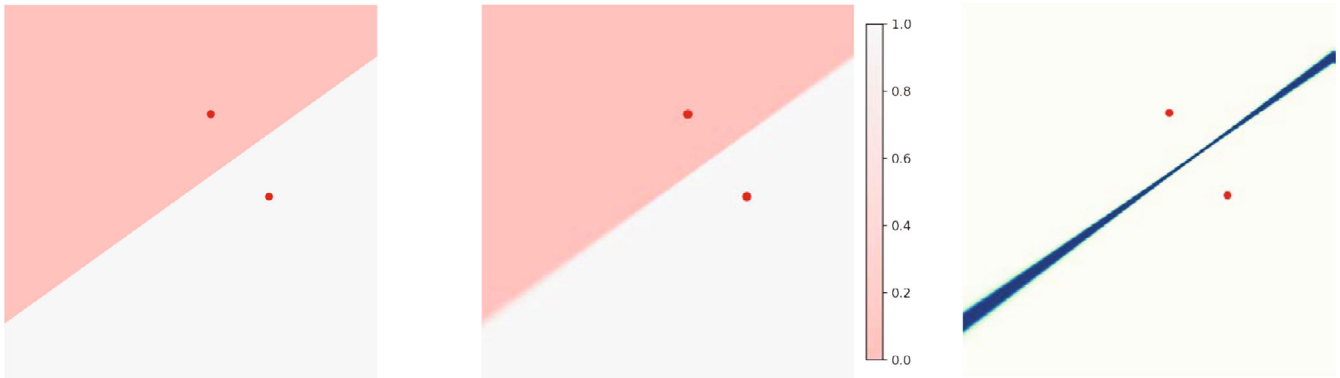

FIGURE 1 Visualization of different quantities formed with two Voronoi points. The red dots indicate the positions of the control points. (A) Standard Voronoi tessellation; (B) Voronoi tessellation using the softmax function; (C) the extracted Voronoi edge between two regions (ρ)

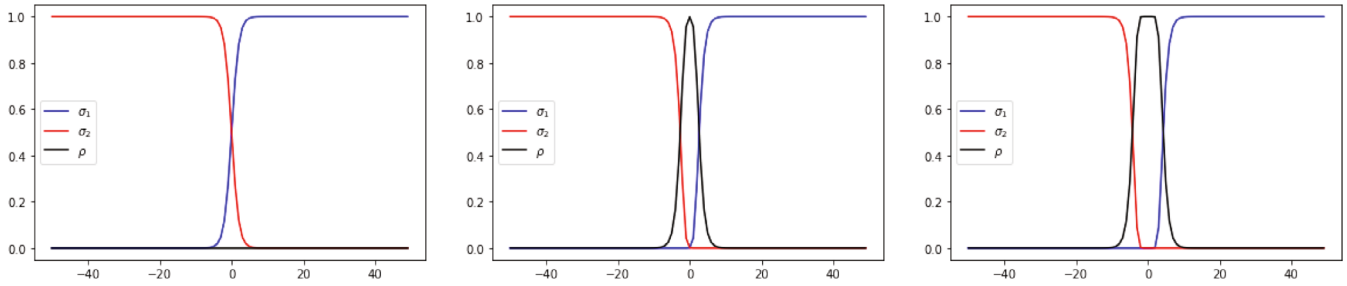

FIGURE 2 Visualization of the softmax function σ_1 (blue), σ_2 (red), and ρ (black) in one dimension with different β values. (A) $\beta = 1$; (B) $\beta = 10$; (C) $\beta = 50$

also increases. We did not treat β as an optimizing variable because there is a more direct relationship between the edge thickness and metric tensor, as discussed in the next subsection.

We remark that the density distribution in Equation (5) defined based on softmax functions in Equation (2) can subdivide the domain into approximate Voronoi cells in which the cell boundaries have a finite thickness as shown in Figure 1C.

2.2 | Anisotropic Voronoi structure

We enhance the local geometric expressiveness by defining the distance metric between points based on Mahalanobis distance[56]

$$\mathrm{d}_m(\boldsymbol{x}, \boldsymbol{x}_m) = \sqrt{(\boldsymbol{x} - \boldsymbol{x}_m)^T \boldsymbol{A}_m (\boldsymbol{x} - \boldsymbol{x}_m)}, \tag{6}$$

where

$$\boldsymbol{A}_m = \boldsymbol{D}_m \boldsymbol{D}_m^T, \tag{7}$$

$\boldsymbol{D}_m$ is a N^d-by-N^d symmetric matrix. This construction ensures that $\boldsymbol{A}_m$ is a positive definite symmetric matrix.

Figure 3 illustrates the difference between isotropic Voronoi tessellation (Figure 3A), anisotropic Voronoi tessellation (Figure 3B) where metric tensors are the same for each control point, and heterogeneous anisotropic Voronoi tessellation (Figure 3C) where metric tensors are different for each control point. Curved edges only form when we have spatially varying metric tensor. It is worth noticing that we use "anisotropic" to feature the geometry of the Voronoi structure characteristics, which only refers to how we define the Voronoi distance, in contrast to the material anisotropy used in continuum mechanics.

2.3 | Voronoi structure with free boundary

We introduce a positive constant ϵ_s to characterize the cellular structure with a free boundary. The key idea is to introduce a universal virtual point that is outside all the current Voronoi points to help defining a Voronoi face that is on the free boundary. In particular, we redefine I_v in (4) and S_m in (2) as

$$I_v = \{0, \ldots, N^c\}, \tag{8}$$

and

$$S_m(\boldsymbol{x}) = f_m^{N^c+1}\left[\epsilon_s, e^{-\mathrm{d}_1(\boldsymbol{x}, \boldsymbol{x}_1)}, \ldots, e^{-\mathrm{d}_{N^c}(\boldsymbol{x}, \boldsymbol{x}_{N^c})}\right], \quad m \in I_v. \tag{9}$$

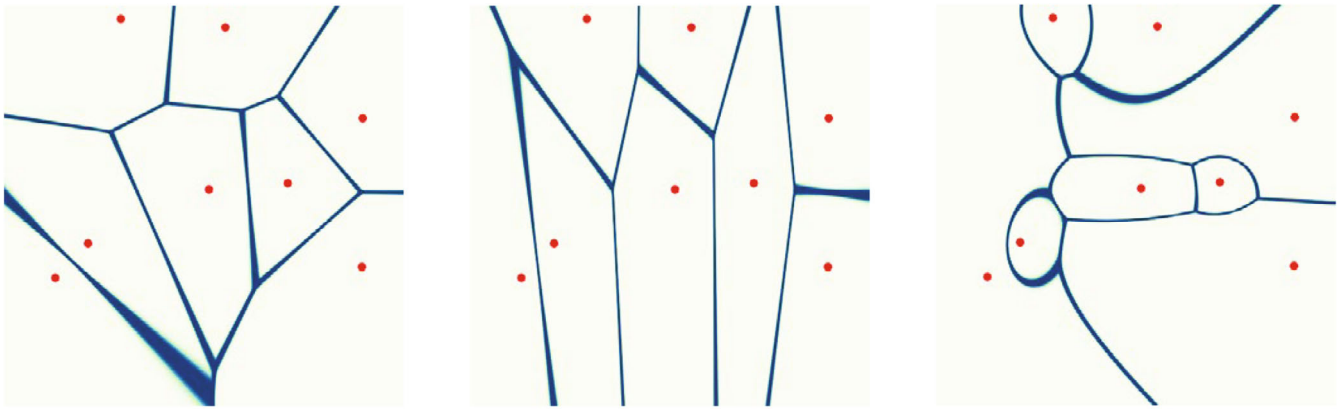

FIGURE 3 Illustration of the anisotropic Voronoi diagram. Domain is a 1×1 square. (A) Isotropic Voronoi diagram with $\boldsymbol{D}_m = [500, 0; 0,500]$; (B) anisotropic Voronoi diagram with $\boldsymbol{D}_m = [750, 0; 0,250]$; (C) heterogeneously anisotropic Voronoi diagram with diagonal entries ranging [0, 1000] and off-diagonal entries ranging $[-50, 50]$

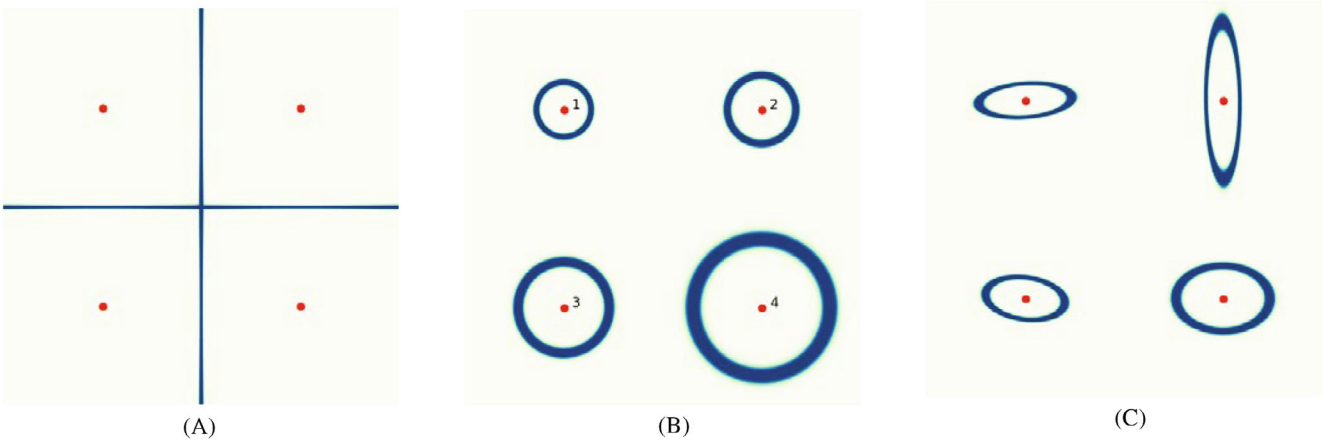

FIGURE 4 Illustration of Voronoi diagram with free boundary. (A) Voronoi cells without free boundaries, equivalent to $\epsilon_s = 0$ with $\boldsymbol{D}_m = 500I$; (B) free boundary cells in different sizes with $\boldsymbol{D}_1 = 500I$, $\boldsymbol{D}_2 = 400I$, $\boldsymbol{D}_3 = 300I$, $\boldsymbol{D}_4 = 200I$ respectively, and $\epsilon_s = 1e-15$; (C) free boundary cells with $\boldsymbol{D}_m$ diagonal entries ranging [0, 1000] and off-diagonal entries ranging $[-50, 50]$

Here, the definition of

$$S_0(\boldsymbol{x}) = \frac{\epsilon_s}{\sum_{n=1}^{N^c} e^{-\mathrm{d}_n(\boldsymbol{x},\boldsymbol{x}_n)} + \epsilon_s}, \tag{10}$$

and

$$S_m(\boldsymbol{x}) = \frac{e^{-\mathrm{d}_m(\boldsymbol{x},\boldsymbol{x}_m)}}{\sum_{n=1}^{N^c} e^{-\mathrm{d}_n(\boldsymbol{x},\boldsymbol{x}_n)} + \epsilon_s}, \tag{11}$$

ensure that ρ in (5) has a compact support.

The effect of free boundary and how different metric tensors influence the sizes and shapes of the cells are illustrated in Figure 4. Figure 4A shows the differentiable Voronoi diagram without free boundary. Figure 4B illustrates the points with different metric tensors D_m forming different sizes of free boundaries. Figure 4C shows cells in different shapes are formed by also using different D_m on each control point.

2.4 | Differentiation of the modified Voronoi partition

The distribution ρ in (5) with (6), (8), and (9) is determined by positions $\boldsymbol{x}_m, m = 1, 2, \dots, N^c$ of the Voronoi centers, matrices $\boldsymbol{D}_m, m = 1, 2, \dots, N^c$ associated with metrics in (7), and one constant ϵ_s. These parameters can generate material distributions with different geometric properties and therefore can be used as design variables that feature a cellular structure. For computing partial derivatives of ρ with respect to parameters $\boldsymbol{x}_m$ and $\boldsymbol{D}_m$, we summarize the results as the following theorem:

Theorem 1. *Assuming ρ is defined by (5) with (6), (8), and (9), its partial derivatives with respect to parameters $\boldsymbol{x}_m, \boldsymbol{D}_m$ can be calculated as*

$$\begin{cases} \frac{\partial \rho(\boldsymbol{x})}{\partial \boldsymbol{x}_n} = -\sum_{m=0}^{N^c} \beta [S_m(\boldsymbol{x})]^{\beta-1} \frac{\partial S_m(\boldsymbol{x})}{\partial \boldsymbol{x}_n}, \ n = 1, 2, \dots, N^c \\ \frac{\partial \rho(\boldsymbol{x})}{\partial \boldsymbol{D}_n} = -\sum_{m=0}^{N^c} \beta [S_m(\boldsymbol{x})]^{\beta-1} \frac{\partial S_m(\boldsymbol{x})}{\partial \boldsymbol{D}_n}, \ n = 1, 2, \dots, N^c, \end{cases} \tag{12}$$

where $\forall m, n = 1, 2, \dots, N^c$,

$$\begin{cases} \frac{\partial S_m(\boldsymbol{x})}{\partial \boldsymbol{x}_n} = S_m(\boldsymbol{x})[S_n(\boldsymbol{x}) - \delta_{mn}]\boldsymbol{Y}_n(\boldsymbol{x}), \\ \frac{\partial S_0(\boldsymbol{x})}{\partial \boldsymbol{x}_n} = S_0(\boldsymbol{x})S_n(\boldsymbol{x})\boldsymbol{Y}_n(\boldsymbol{x}), \\ \frac{\partial S_m(\boldsymbol{x})}{\partial \boldsymbol{D}_n} = S_m(\boldsymbol{x})[S_n(\boldsymbol{x}) - \delta_{mn}]\mathrm{d}_n(\boldsymbol{x}, \boldsymbol{x}_n)\left[\boldsymbol{X}_n(\boldsymbol{x}) \otimes \boldsymbol{X}_n(\boldsymbol{x})\right]\boldsymbol{D}_n, \\ \frac{\partial S_0(\boldsymbol{x})}{\partial \boldsymbol{D}_n} = S_0(\boldsymbol{x})S_n(\boldsymbol{x})\mathrm{d}_n(\boldsymbol{x}, \boldsymbol{x}_n)\left[\boldsymbol{X}_n(\boldsymbol{x}) \otimes \boldsymbol{X}_n(\boldsymbol{x})\right]\boldsymbol{D}_n. \end{cases} \tag{13}$$

Here,

$$\begin{cases} \boldsymbol{X}_n(\boldsymbol{x}) = \frac{\boldsymbol{x}_n - \boldsymbol{x}}{\mathrm{d}_n(\boldsymbol{x}, \boldsymbol{x}_n)}, \ n = 1, 2, \dots, N^c, \\ \boldsymbol{Y}_n(\boldsymbol{x}) = \boldsymbol{A}_n(\boldsymbol{x})\boldsymbol{X}_n(\boldsymbol{x}), \ n = 1, 2, \dots, N^c, \end{cases} \tag{14}$$

and δ_{mn} is the Kronecker delta function

$$\delta_{mn} = \begin{cases} 1, & m = n, \\ 0, & m \neq n. \end{cases} \tag{15}$$

Proof. Equation (12) can be derived directly from the chain rule and (5). Next, we prove (13). From (9), we have $\forall m, l = 1, 2, \dots, N^c$

$$\begin{cases} \frac{\partial S_m}{\partial \mathrm{d}_l(\boldsymbol{x}, \boldsymbol{x}_l)} = S_m\left(S_n - \delta_{ml}\right), \\ \frac{\partial S_0}{\partial \mathrm{d}_l(\boldsymbol{x}, \boldsymbol{x}_l)} = S_0 S_l. \end{cases} \tag{16}$$

Taking the partial derivatives of (6) yields

$$\begin{cases} \frac{\partial \mathrm{d}_l(\boldsymbol{x}, \boldsymbol{x}_l)}{\partial \boldsymbol{x}_n} = \delta_{ln}\boldsymbol{Y}_n, \\ \frac{\partial \mathrm{d}_l(\boldsymbol{x}, \boldsymbol{x}_l)}{\partial \boldsymbol{D}_n} = \delta_{ln}\mathrm{d}_n(\boldsymbol{x}, \boldsymbol{x}_n)[\boldsymbol{X}_n(\boldsymbol{x}) \otimes \boldsymbol{X}_n(\boldsymbol{x})]\boldsymbol{D}_n, \end{cases} \tag{17}$$

Combining (16) and (17) using the chain rule yields (13). ∎

3 | TOPOLOGY OPTIMIZATION

3.1 | Incorporating Voronoi to topology optimization

In topology optimization, we store the density and projected density distributions ρ on a structured Cartesian grid in domain Ω, the density and projected density distributions at each grid point are denoted as $\rho_e, e = 1, \dots, N^e$. Without causing ambiguity, we also denote ρ and as vectors consisting of all discrete ρ_e respectively. Following Reference 57, we write a topology optimization problem as the minimization of the mean compliance $c(\boldsymbol{x}, \boldsymbol{D})$ for the filtered density distribution $\tilde{\rho}$ in the nested formulation

$$minimize_{\boldsymbol{x},\boldsymbol{D}} \quad c(\boldsymbol{x}, \boldsymbol{D}) := \boldsymbol{F}^T \boldsymbol{U} \quad \text{subject to} \quad \frac{V(\tilde{\rho})}{V(\Omega)} \leq \bar{f}, \tag{18}$$

where $\tilde{\rho} = f_H(\rho) \equiv \frac{\tanh(\gamma\eta) + \tanh(\gamma(\rho-\eta))}{\tanh(\gamma\eta) + \tanh(\gamma(1-\eta))}$ is the relaxed Heaviside projection[58] with threshold $\eta = 0.5$ and γ starting from 1 doubled every 50 frames, gradually producing a more binary filtered density field. $\boldsymbol{F}$ is the external force vector, $\boldsymbol{U}$ is the global displacement vector, $V(\tilde{\rho})$ is the material volume, $V(\Omega)$ is the volume of the design domain Ω, and $\bar{f}$ is the prescribed volume fraction. Design variables are the positions $\boldsymbol{x}$ and metric tensors $\boldsymbol{D}$ of the site points. $\boldsymbol{x}$ takes a range at least three times as large as the design domain on each axis (i.e., Voronoi points can be positioned outside of the design domain and not form density inside, thus not influencing the final structure). The diagonal entries in $\boldsymbol{D}$ takes a range as large as $[0, 2000]$, where larger range produces a more variation in edge thickness, and the off-diagonal terms in $\boldsymbol{D}$ has range $[-100,100]$. The global displacement vector $\boldsymbol{U}$ is obtained by solving the following force equilibrium

$$\boldsymbol{K}(\boldsymbol{x}, \boldsymbol{D})\boldsymbol{U} = \boldsymbol{F}, \tag{19}$$

where $\boldsymbol{K}$ is the global stiffness matrix.

Following the modified SIMP method, the stiffness matrix of each grid element is interpolated as follows,

$$\begin{aligned} E_e &= E_{\min} + \tilde{\rho}_e^p (E_0 - E_{\min}), \\ \boldsymbol{k}_e &= E_e \boldsymbol{k}_0, \end{aligned} \tag{20}$$

where E_e is the interpolated Young's modulus of each element, E_0 is the Young's modulus of a completely solid element, $E_{\min}$ is a very small value to prevent singularity of the global stiffness matrix and $\boldsymbol{k}_0$ is the element stiffness matrix given by $\boldsymbol{k}_0 = \int_V \boldsymbol{B}^T \boldsymbol{E} \boldsymbol{B}\, dV$ with Young's modulus equal to 1. In the analytical expression of $\boldsymbol{k}_0$, V is the volume of one element, $\boldsymbol{B}$ is the strain displacement Matrix and $\boldsymbol{E}$ is the stress–strain matrix. One can form the element stiffness matrix through Gaussian quadrature discretization or a pre-calculated matrix. We refer readers to References 59 and 60 for the formulation of the element stiffness matrix in 2D and 3D respectively. We assemble $\boldsymbol{K}$ as a sparse matrix by filling in the entries of nodes associated with each element stiffness matrix. Here we choose the penalizing power $p = 1$ because our Voronoi formulation forms relatively binary pattern by its definition.

3.2 | Sensitivity analysis

The sensitivity analysis is given as followings using chain rule

$$\begin{cases} \frac{\partial c}{\partial \boldsymbol{x}_m} = \sum_e \frac{\partial c}{\partial \tilde{\rho}_e} \frac{\partial \tilde{\rho}_e}{\partial \rho_e} \frac{\partial \rho_e}{\partial \boldsymbol{x}_m}, \\ \frac{\partial c}{\partial \boldsymbol{D}_m} = \sum_e \frac{\partial c}{\partial \tilde{\rho}_e} \frac{\partial \tilde{\rho}_e}{\partial \rho_e} \frac{\partial \rho_e}{\partial \boldsymbol{D}_m}, \\ \frac{\partial V}{\partial \boldsymbol{x}_m} = \sum_e \frac{\partial V}{\partial \tilde{\rho}_e} \frac{\partial \tilde{\rho}_e}{\partial \rho_e} \frac{\partial \rho_e}{\partial \boldsymbol{x}_m}, \\ \frac{\partial V}{\partial \boldsymbol{D}_m} = \sum_e \frac{\partial V}{\partial \tilde{\rho}_e} \frac{\partial \tilde{\rho}_e}{\partial \rho_e} \frac{\partial \rho_e}{\partial \boldsymbol{D}_m}, \end{cases} \tag{21}$$

where

$$\begin{cases} \frac{\partial c}{\partial \tilde{\rho}_e} = -p\tilde{\rho}_e^{p-1}(E_0 - E_{\min})u_e^T k_0 u_e, \\ \frac{\partial \tilde{\rho}_e}{\rho_e} = \gamma \frac{1-\tanh(\gamma(\rho_e-\eta))^2}{\tanh(\gamma\eta)+\tanh(\gamma(1-\eta))}, \end{cases} \tag{22}$$

and $\partial\rho_e/\partial \boldsymbol{x}_m, \partial\rho_e/\partial \boldsymbol{D}_m$ are defined as (12).

4 | IMPLEMENTATION

4.1 | Neighbor search

The computation cost is high for calculating the gradients with respect to $\boldsymbol{x}$ and $\boldsymbol{D}$, since it involves double loops as shown in (12), (13) as both m and n need to iterate from 1 to N^c. The computation cost is therefore $O((N^c)^2)$ for each $\frac{\partial \rho_e}{\partial \boldsymbol{x}}$ and $\frac{\partial \rho_e}{\partial \boldsymbol{D}}$. However, only limited Voronoi points influence a grid element to form a high-density area as the softmax function finds the minimum distance to a given grid point and the edges are formed in areas where the minimum distances to multiple Voronoi points are similar. Therefore, the computation cost can be reduced to $O(k^2)$ if we only loop through k Voronoi points closest to the grid element, and the added cost for searching k-nearest neighbor is $O(k \log N)$. Thus, we find k-nearest neighbors every time before we compute the density formed by the Voronoi points and only use the k-nearest neighbors also to compute the gradients. The sensitivity calculation is the performance bottleneck of our current implementation. As shown in Figure 5, there is a linear relationship between number k and computational cost of Voronoi density calculation (Algorithm 1) and a quadratic relationship between number k and Voronoi gradients calculation (Algorithm 2), with significantly more time cost on the gradient calculation part. We use k in the range from 7 to 20 for numerical examples to accommodate examples with high anisotropy.

4.2 | Workflow

Overall our method has a similar optimization procedure as that of SIMP. However, our method uses Voronoi design variables $\boldsymbol{D}_m$ and $\boldsymbol{x}_m$ instead. We solve the continuous optimization problem defined by (18) using a gradient-based, iterative optimization scheme. Four major steps are computed in each iterative step. First, we need to calculate the density ρ based on the positions $\boldsymbol{x}_m$ and the metric tensors $\boldsymbol{D}_m$, as shown in Algorithm 1. Second, we perform the FEM solve using an MGPCG (multi-grid preconditioned conjugate gradient) solver to obtain displacement $\boldsymbol{u}$ of each element and calculate the corresponding compliance c. Third, we compute the gradients of compliance c and volume V with respect to $\boldsymbol{D}_m$ and $\boldsymbol{x}_m$. For clarification, we give the pseudo-code of calculating $\frac{\partial c}{\partial \boldsymbol{x}}$ using neighbor search in Algorithm 2, the other gradients are calculated similarly. Last, we update the design variables using the method of moving asymptotes method (MMA).[61,62] The pseudo-code of our overall workflow is given in Algorithm 3.

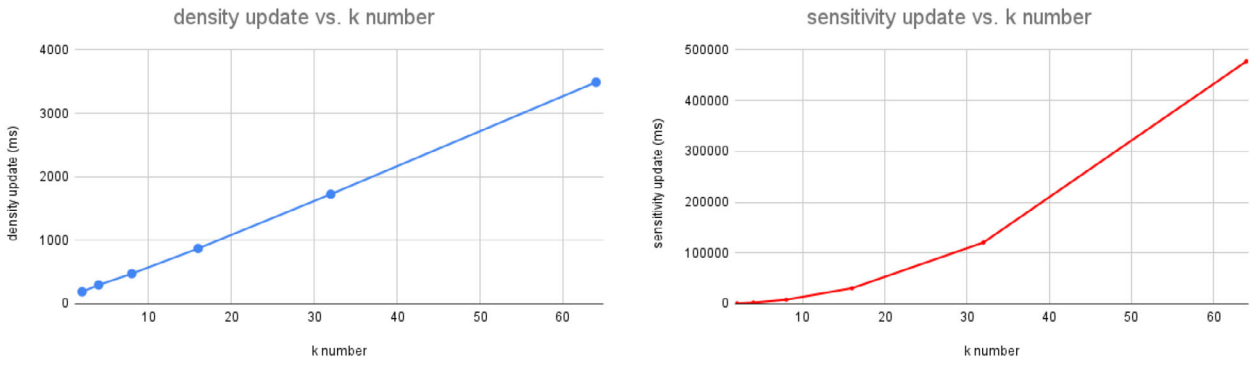

FIGURE 5 Computational cost density update and sensitivity update versus k number in a 1024×1024 grid with 256 Voronoi points.

Algorithm 1. Calculation of differentiable Voronoi diagram

Input: Positions Voronoi points $\boldsymbol{x}$, Metric tensor $\boldsymbol{D}$
Output: Neighbors field *nbs*, Density field ρ

for $i \leftarrow 0$ to N^c **do** ▷ update $\boldsymbol{A}$
  $\boldsymbol{A}[i] = \boldsymbol{D}[i]@\boldsymbol{D}[i].T$
end for
for $i \leftarrow 0$ to N^e **do** ▷ update neighbors
  $nbs[i] \leftarrow$ Find_K_Nearest_Nb($\boldsymbol{x}_i, \boldsymbol{x}$) ▷ stores the index of the ith neighbor
end for
for $i \leftarrow 0$ to N^e **do** ▷ update denominator in Equation (11)
  for $j \leftarrow 0$ to k **do**
    $Sum \leftarrow Sum + \exp(-d(\boldsymbol{x}_i, \boldsymbol{x}_{nbs[i][j]}))$
  end for
  $softmax_sum[i] \leftarrow Sum + \epsilon_s$ ▷ store the intermediate softmax sum in a field
end for
for $i \leftarrow 0$ to N^e **do** ▷ update ρ
  for $j \leftarrow 0$ to k **do**
    $\rho_i \leftarrow 1 - \left[\exp\left(\frac{-d(\boldsymbol{x}_i, \boldsymbol{x}_{nbs[i][j]})}{softmax_sum[i]}\right)\right]^{\beta}$
  end for
end for

Algorithm 2. Calculation of $\partial\rho/\partial\boldsymbol{x}$

Input:field of int array *nbs*, field $\frac{\partial c}{\partial \tilde{\rho}_e}$ and $\frac{\partial \tilde{\rho}_e}{\partial \rho_e}$
Output: derivative of compliance with respect to Voronoi point positions $\frac{\partial c}{\partial \boldsymbol{x}}$

for $e \leftarrow 0$ to N^e **do** ▷ calculate $\frac{\partial \rho_e(\boldsymbol{x})}{\partial \boldsymbol{x}_{nbs[e][m]}}$, parallelizable
  for $m \leftarrow 0$ to k **do**
    $\frac{\partial \rho_e(\boldsymbol{x})}{\partial \boldsymbol{x}_{nbs[e][m]}} \leftarrow \boldsymbol{0}$
    for $n \leftarrow 0$ to k **do**
      $\frac{\partial S_{nbs[e][m]}(\boldsymbol{x})}{\partial \boldsymbol{x}_n} \leftarrow S_{nbs[e][m]}(\boldsymbol{x})[S_{nbs[e][n]}(\boldsymbol{x}) - \delta_{(nbs[e][m])(nbs[e][n])}]\boldsymbol{Y}_{nbs[e][n]}(\boldsymbol{x})$ ▷ Equation (13)
      $\frac{\partial \rho_e(\boldsymbol{x})}{\partial \boldsymbol{x}_{nbs[e][m]}} -= \beta \left[S_{nbs[e][m]}(\boldsymbol{x})\right]^{\beta-1} \frac{\partial S_{nbs[e][m]}}{\partial \boldsymbol{x}_{nbs[e][n]}}$ ▷ Equation (12)
    end for
  end for
end for
for $e \leftarrow 0$ to N^e **do** ▷ calculate $\frac{\partial c}{\partial \boldsymbol{x}_{nbs[e][m]}}$, not parallelizable
  for $m \leftarrow 0$ to k **do**
    $\frac{\partial c}{\partial \boldsymbol{x}_{nbs[e][m]}} += \frac{\partial c}{\partial \tilde{\rho}_e}\frac{\partial \tilde{\rho}_e}{\partial \rho_e}\frac{\partial \rho_e}{\partial \boldsymbol{x}_{nbs[e][m]}}$ ▷ (21)
  end for
end for

Algorithm 3. Topology optimization with differentiable Voronoi diagrams

Input: Volume fraction f, Number of Voronoi points N^c, Metric tensor $\boldsymbol{D}$
Output: Density field $\tilde{\rho}$

Initialize positions of Voronoi points $\boldsymbol{x}$ randomly in a coarse grid
Iteration counter $i = 0$
Design variable change $\Delta = 1$
Projection parameter $\beta = 1$
while $i < i_{\max}$ and $\delta > 1e-4$ **do**
  Calculate ρ ▷ Equation (5), Algorithm 1
  Density projection $\tilde{\rho} \leftarrow \rho$
  Compute compliance c ▷ Equations (18) and (20)
  Calculate $\frac{\partial c}{\partial \boldsymbol{D}}, \frac{\partial c}{\partial \boldsymbol{x}}, \frac{\partial V}{\partial \boldsymbol{x}}, \frac{\partial V}{\partial \boldsymbol{D}}$ ▷ Equation (21), Algorithm 2
  Update $\boldsymbol{D}$ and $\boldsymbol{x}$ with MMA optimizer
  $\Delta = \max\{\max_{\forall m}(|\boldsymbol{D}_m^i - \boldsymbol{D}_m^{i-1}|), \max_{\forall m}(|\boldsymbol{x}_m^i - \boldsymbol{x}_m^{i-1}|)\}$
  $i = i + 1$
end while

5 | NUMERICAL RESULTS

We discuss the numerical results obtained using our approach. For all the examples, we assume isotropic elasticity specified by Young's modulus $E = 1$ and Poisson's ratio $\mu = 0.3$. In the optimization, the lower bound of Young's modulus $E_{\min}$ is $1e-9$. We use $\beta = 50$ for the Voronoi representation. We conduct all of our numerical examples on a regular lattice grid with square elements in 2D and cube elements in 3D. Ideally, we assume that we have an unlimited resolution of the background grid. However, with the limited computational resource, the finite element size should be at most half of the thickness of Voronoi edges. Our experiments consists in four parts, including the ablation tests (Section 5.1), standard tests (Section 5.2), biomimetic applications (Section 5.3), free-boundary examples (Section 5.4), and three-dimensional results (Section 5.5).

5.1 | Ablation tests

We first conduct two ablation tests to verify the roles of position $\boldsymbol{x}_m$ and metric tensor $\boldsymbol{D}_m$ separately. Both experiments were carried out with two Voronoi points on a 512×512 grid. We first test the optimization of $\boldsymbol{x}_m$ (see Figure 6). The boundary condition is set as a distributive force within a narrow region on the top and the bottom nodes being fixed. We initialize the position of two Voronoi points randomly as shown in Figure 6B, where a tilted beam is formed, not connected with any fixed nodes on the bottom. The metric tensor D for each Voronoi point is set to be 80 multiplying an identity to ensure an appropriate edge thickness. After convergence, as shown in Figure 6C, the beam is rotated to the middle of the domain by the moving control points, connecting the force load and the fixed base to minimize the structure's compliance. We set up a similar optimization problem as in Figure 7A to verify the role of $\boldsymbol{D}_m$. The bottom-left and the bottom-right corners are fixed and an external load is applied in the center. We initialize two Voronoi points with their position fixed and only optimize for their metric tensor. The program obtains $\boldsymbol{D}_1 = [282, 1.4e-4; 1.4e-4, 89]$ for the lower point and $\boldsymbol{D}_2 = [228, -1.3e-4; -1.3e-4,106]$ for the higher point after convergence. The optimized design forms an arch to minimize the compliance while satisfying the pre-defined target volume constraints. The two tests jointly show that both design variables are effective in guiding the structure to evolve to a low-compliance status.

5.2 | Standard tests

We optimize $\boldsymbol{x}$ and $\boldsymbol{D}$ for cellular cantilever beam structures with a minimum compliance. The optimized design after 245 iterations is shown in Figure 8A. We first randomly initialize 18 points in a 6×3 coarse grid of a 512×256 domain with an initial $\boldsymbol{D} = [150, 0;\ 0,150]$. Our optimized structure resembles that of a standard topology optimization result, Figure 8B,

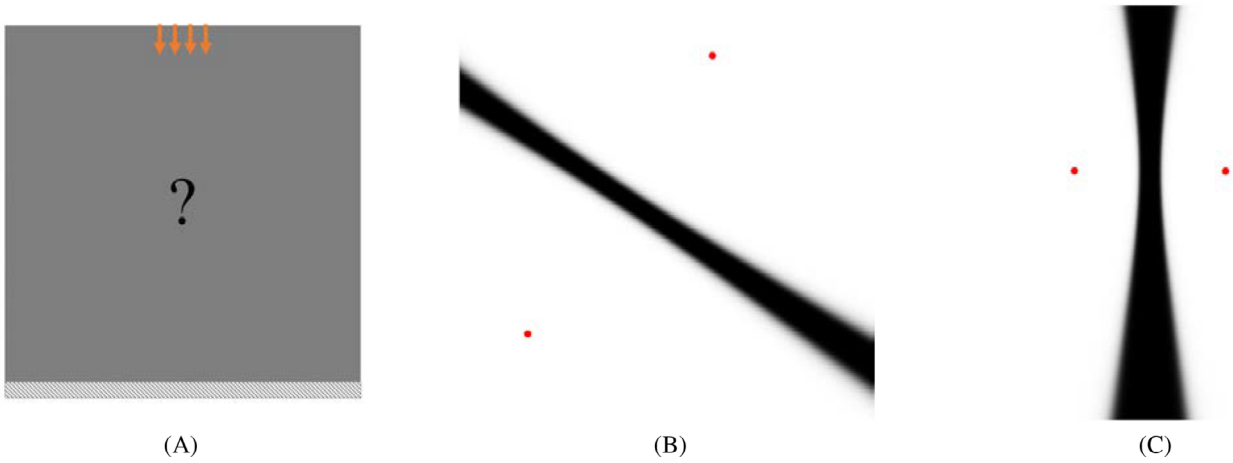

FIGURE 6 (A) Setup for the pushdown experiment. (B) Initial density distribution. (C) Density distribution after optimization. The red points indicate the positions of two Voronoi points.

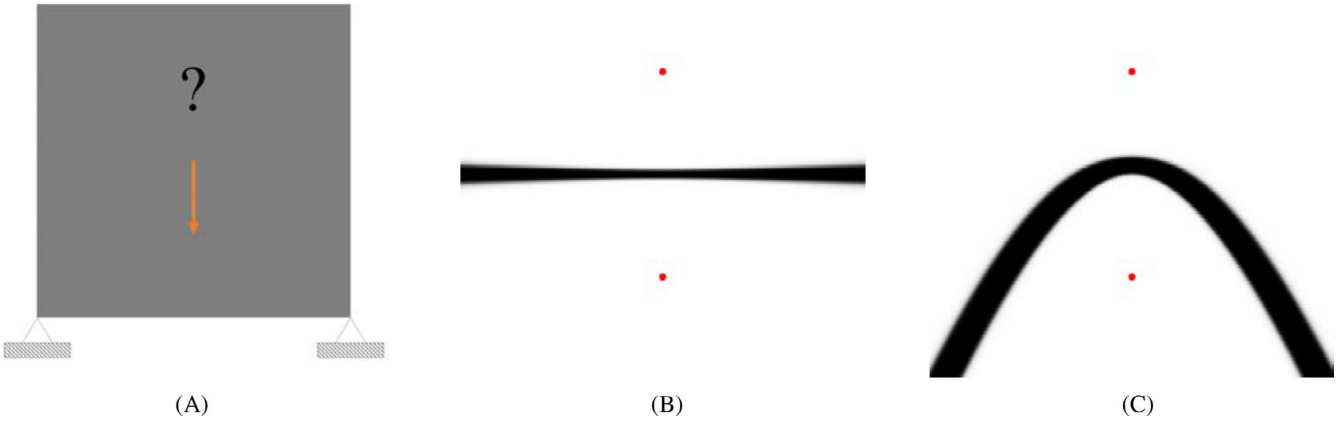

FIGURE 7 (A) Setup for the middle drag experiment. (B) Initial density distribution. (C) Density distribution after optimization. The red points indicate the positions of two Voronoi points.

as the long beams are formed both on the bottom and top, connecting the fixed boundary with the loads. We did not visualize Voronoi points outside the domain, which also contribute to the structure. The compliance of our structure is 5.5% above the one obtained by the standard method. We conjecture that the slightly larger compliance is in part due to the waste materials formed on the top right corner, which is not contributing to lower the compliance and the constrained design space for cellular patterns. We show a comparable optimization convergence performance as the standard SIMP method (see Figure 8C), in which both methods converge within 150 frames. We conjecture the spikes in the objective curve to be caused by a relatively significant change in density distribution when the positions/metric tensors change mildly in value. These jitters can be mitigated by further decreasing the move limits of the optimization parameters.

The second example is a framed cantilever beam with a distributed force load. The nodes on the left side are all fixed, and downward-pointing forces are exerted in the middle region on the right side, occupying the middle 20% of the total height. The rectangular frame of the 1×0.5 domain is fixed to be filled with solid materials with a beam thickness of 0.01 (in the framed cases). The target volume is set to be 0.35. The optimization results with the different number of initial points are shown in Figure 9. From left to right, we observe that a more distributed structure is formed with more Voronoi points. All optimized structures form axial beams that traverse from the left top corner to the right middle, similarly, from the left bottom corner to the right middle. Additionally, both form the dark "anchor" regions on the top left and bottom left corners. These features demonstrate the spatially adaptive nature of our method, which are also the keys to minimizing the compliance in this boundary setup. Comparing the upper row without density on the frame and the lower row with density on the frame, the overall structures look similar except that there are less material connecting to the upper and

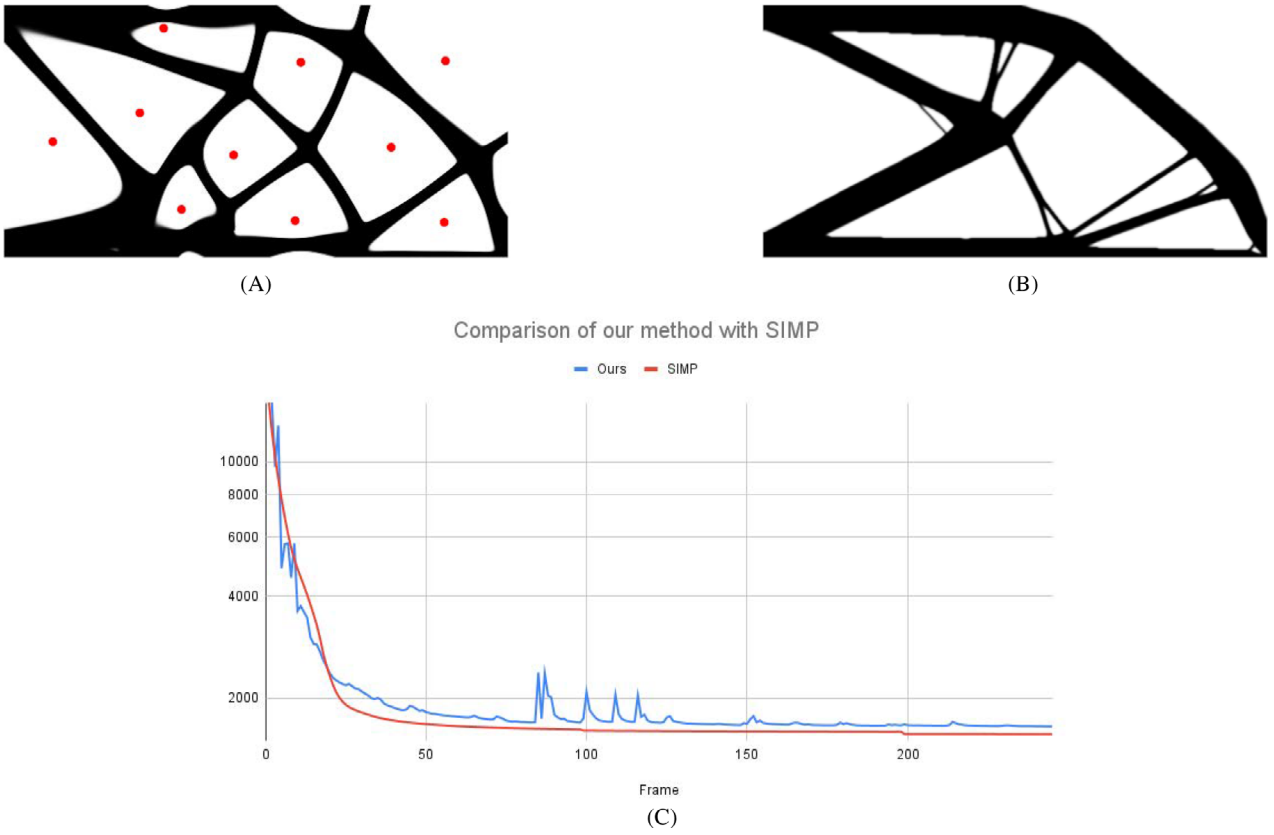

FIGURE 8 Optimization results of two-dimensional cantilever beams. (A) Our result. (B) Result obtained using SIMP. (C) The objective convergence comparison.

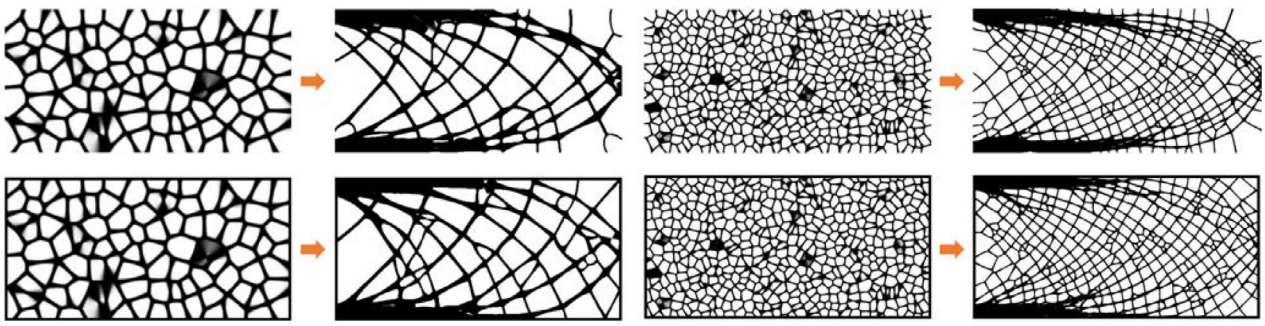

FIGURE 9 Topology optimization of Voronoi structures with distributed force load on the right side. The top row shows the results without density on the boundary while the bottom row shows the result that has one layer of density on the boundary. The left side is the result formed by 98 Voronoi points with resolution 512×256 while the results on the right side are formed by 512 Voronoi points with a grid resolution of 1024×512.

lower corner in the examples without frame. For the results in the 512×256 grid, 17 Voronoi points move to outside of the domain in both cases. For the results in the 1024×512 grid, 83 Voronoi points move to outside of the active cell domain for the case where density fills the frame while 98 points move to outside of the domain for the unframed case.

In Figure 10, we initialize the points in the centers of the coarse grids. Since the stress distribution is symmetric across the horizontal axis, the optimization initialization of points in the 14×7 coarse grid exhibits asymmetrical pattern as early as frame 1. When we optimize the structure with initialization of points in the 16×8, it preserves a symmetric structure until frame 13. Also, we observe that starting from frame 13, the volume constraint is better satisfied. So we conclude that the optimizer prioritize satisfying volume constraint than strictly following gradient from that point on.

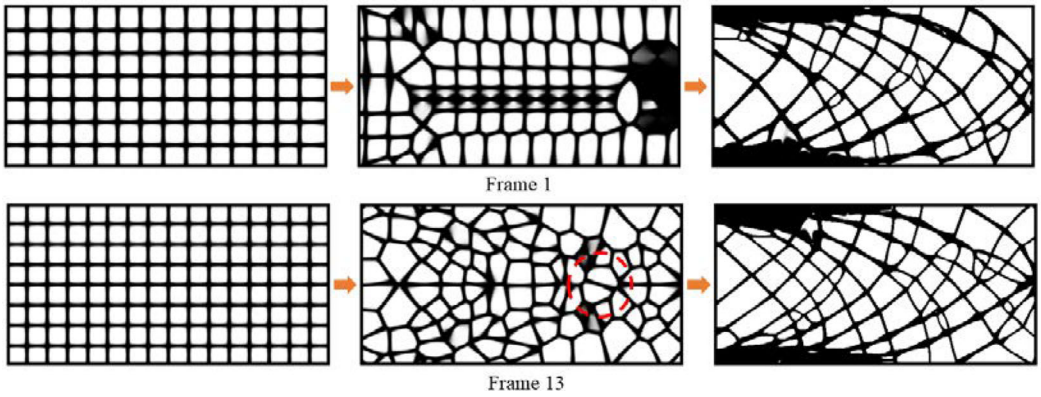

FIGURE 10 Optimization result of the framed cantilever beam with 14×7 and 16×8 points respectively.

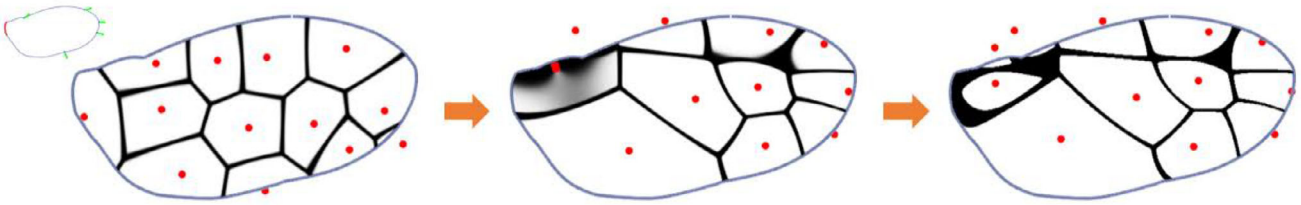

FIGURE 11 Evolution of Voronoi points and corresponding density for the Diptera wing example. From left to right at iteration 1, 100, and 299 respectively. The boundary condition is illustrated on the inset picture on the top left, where the red points indicate the fixed nodes, blue points indicate the nodes that receive forces, and the green lines indicate the force directions.

5.3 | Biomimetic structures

To demonstrate the efficacy of our approach in optimizing biomimetic cellular structures, we optimize the structure within a Diptera wing contour as in Figure 11. We randomly initialize 13 Voronoi points in a 6×3 grid with $\boldsymbol{D} = [400, 0;\ 0{,}400]$. The target volume fraction is set to 0.15. For processing the irregular boundary here, we first convert a silhouette of the Diptera wing shape into a level set field using fast marching algorithm.[63] Then, we mark the cells with negative level set values as active and mark the cells with positive level set values as inactive cells, which we set $\rho_e = 0$ and do not optimize the density distribution. The nodes that have active neighbor cells and inactive neighbor cells are marked as boundary nodes and we apply boundary forces on them. The directions of the boundary forces are partially determined by the gradient of the level set as well. As shown in Figure 11, the Voronoi points are distributed in the design domain evenly and the initial Voronoi tessellation is similar to a CVT. As optimization proceeds, however, the Voronoi partitions are more elongated, which conforms to the force direction. Also, the beams on the left side connecting to the fixed points are relatively thicker than the beams on the right side. Note that although some regions with diffused density appear as two points closer to each other, they separate naturally in the later iterations after the stronger filter strength leads to a more binary density pattern. A denser cellular pattern in an Odonata front wing is shown in Figure 12, where 290 points with an initial $\boldsymbol{D} = [1300, 0;\ 0, 1300]$ and 1116 points with an initial $\boldsymbol{D} = [2600, 0;\ 0, 2600]$ are optimized after 249 iterations. The irregular boundary is set similarly in this example except that the cells within a certain positive epsilon values are marked as boundary cells with $\rho_e = 1$, and the boundary nodes are in between boundary and inactive cells. It can be observed that thick beams are formed towards the fixed nodes on the right side and there is a spectrum of variations in the edge thickness.

We also test our algorithm to optimize a bone's interior. As illustrated in Figure 13, we fix the bottom of the bone shape and add distributed pulling forces on the top left and distributed pushing force on the top right. The evolution of the topology optimization process is shown in Figure 13 at selected frames. We can see that the overall density of distribution is reached as early as iteration 50, while a more binary and refined structure is achieved in the end. Our results are consistent with the characteristic femur bone structure with elongated cells and inhomogeneous density distribution across the entire domain. The result formed with 773 points has a more distributed density while maintaining the overall

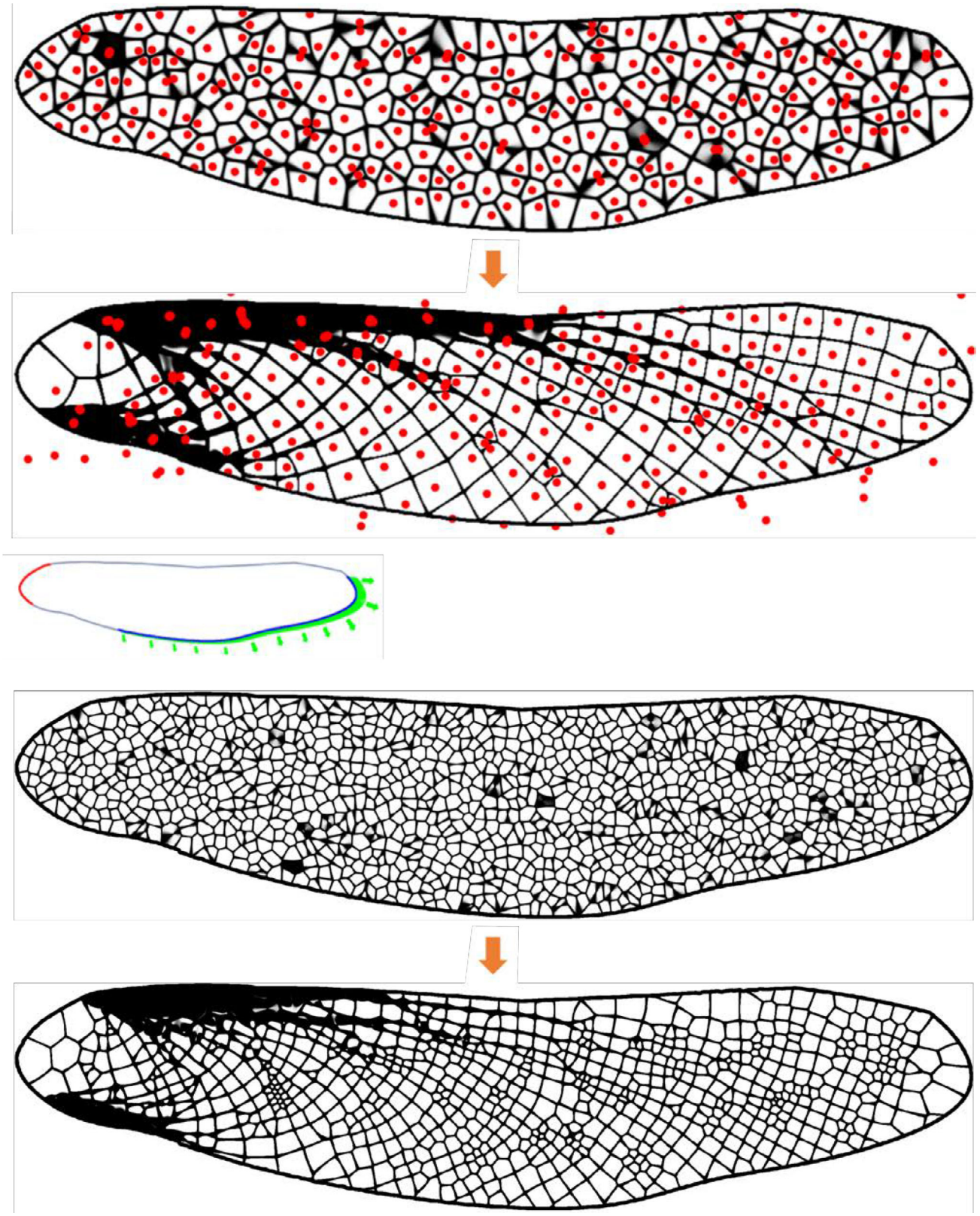

FIGURE 12 The evolution result of Odonata front wing. The boundary condition is illustrated in the inset picture on the middle left. Top row: The optimized design with 290 Voronoi points in a 1024×256 domain. Bottom row: The optimized design with 1116 Voronoi points in a 2600×650 domain.

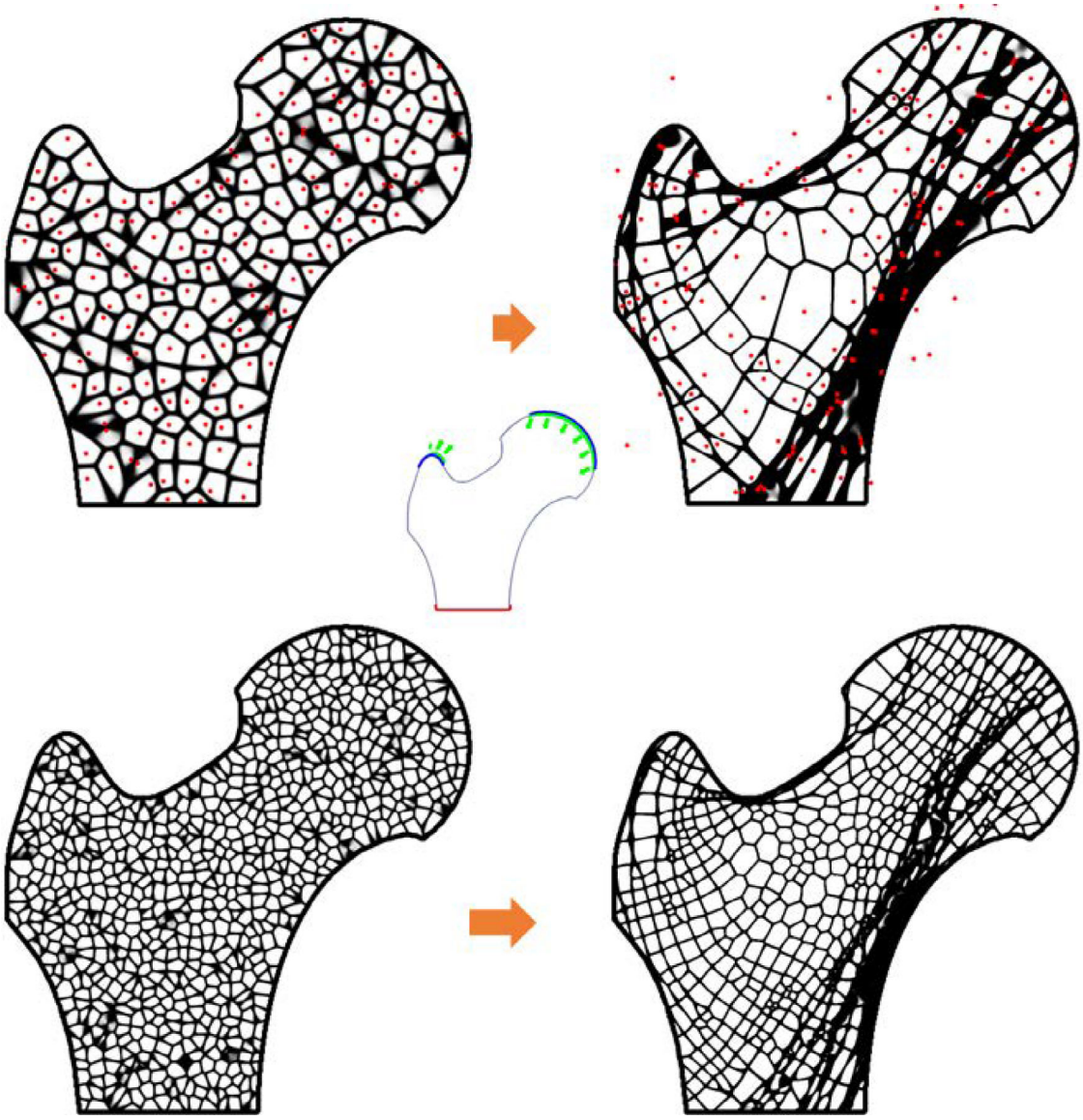

FIGURE 13 Evolution of cellular structures for the bone example. Middle: Boundary condition for the bone example. Similar to the Diptera example, the darker blue contour indicates the boundary of the design domain. The red nodes on the bottom are the fixed nodes. The distributed forces are applied to the two locations indicated by blue circles with green bars attached, which visualize the direction and the strength of the forces. Top row: Left is the initialization of 196 Voronoi points on a 1024×1024 grid and Right is the optimized result after 249 iterations. Bottom row: Left is the initialization of 773 Voronoi points on a 1024×1024 grid and Right is the optimized result after 249 iterations.

cellular directions. In this example, the structure formed with fewer points achieves a lower compliance 102 than that of the structure formed by more points (115) which implies that a less even density distribution is more desirable under this specific boundary condition.

5.4 | Foam structures with free boundary

Our method is also capable of optimizing foam structures with free boundaries, ergo, no need to connect cell walls all the way to the border of the design domain, thus forming cellular structures seen in nature such as cell clusters. In this subsection, we demonstrate the unprecedented cellular structure with/without enabling the anisotropic feature. All experiments are done with the standard cantilever beam boundary condition.

In Figure 14, we optimize only the positions of the Voronoi control points. On a 512×256 grid, we initialize 32 points and 98 points randomly in coarse grids 8×4 and 14×7, respectively. The initial $\boldsymbol{D}$ is set to [250, 0; 0,250] for the experiment with fewer points, and [350, 0; 0,350] for the experiment with more points. The value of ϵ_s is set to $1e-7$ to obtain an appropriate radius for the cell size. In the beginning, the cells spread out the entire domain, without a structure. After 15 iterations, cells start to cluster in order to form a long beam connecting the left fixed side with the force load on the right bottom corner. A more clear 2-beam structure forms at the 50th iteration, and final structures that more resemble a standard cantilever beam form in the end. Notice that since there is no structure connecting the force load and the fixed nodes in the beginning, the FEM solve does not converge. However, the optimization process is not obstructed by this issue.

With the same initial setup, but enabling the optimization of $\boldsymbol{D}$, we can obtain cellular structures with morphed cells and lower compliance as shown in Figure 15. Similarly, the cells are dispersed randomly in a coarse grid at the start point and start to form beam structures with less distorted cells at iteration 15. The structure at iteration 50 consists of more distorted cells while maintaining the overall structure. In the end, thicker beams are formed on the bottom and across from the left-top to the bottom right corner for both cases.

In Figure 16, we compare the compliance function curves of the cellular structures with free boundary formed only optimizing $\boldsymbol{x}$ and optimizing both $\boldsymbol{x}$ and $\boldsymbol{D}$ with 32 and 98 Voronoi points respectively. In both cases, the structures obtained by optimizing both $\boldsymbol{x}$ and $\boldsymbol{D}$ reach much lower compliance values.

Furthermore, we compare the compliance of the structure with free boundaries and without free boundaries as shown in Figure 17. In this case, the final compliance of the structure with free boundaries is higher than that without free boundaries, even though the structure with the free boundary removes the extra material on the upper right corner that does not contribute to lowering the compliance. This is the constraint of the free boundary structure as the cells need to form a closed cellular structure and there are no connecting cells with the fixed nodes on the left side under this volume constraint.

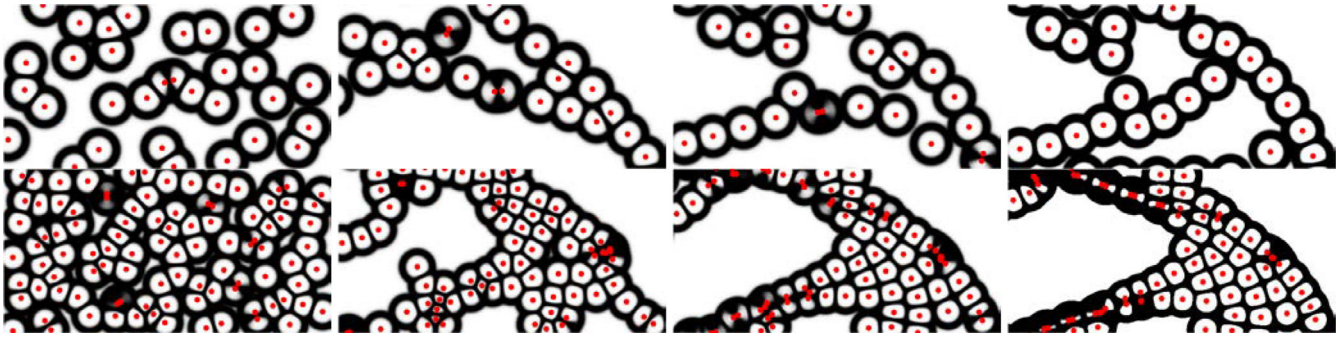

FIGURE 14 Cellular structure with free boundary, only optimizing x. From left to right, the columns are optimization results at iteration 0, 15, 50, and 249 respectively. The top row is the result formed by 32 Voronoi points while the results on the bottom are formed by 98 Voronoi points.

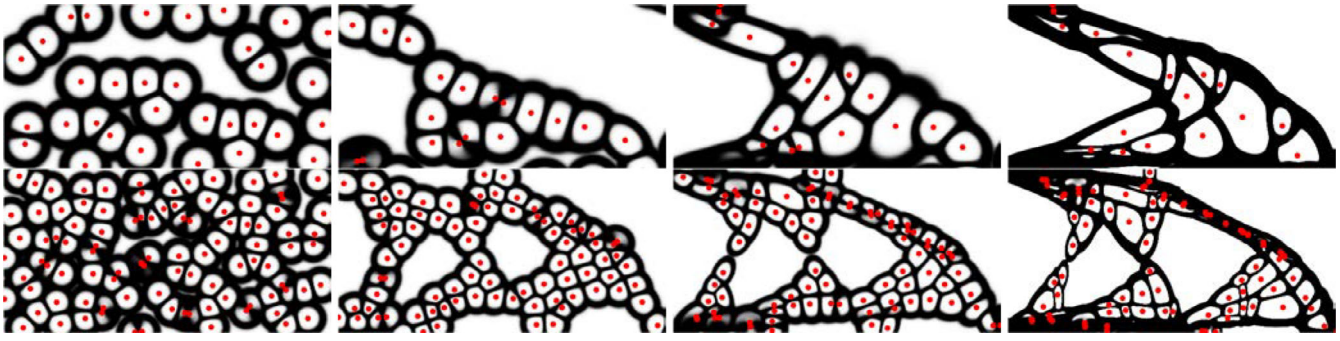

FIGURE 15 Anisotropic cellular structure with free boundary, optimizing both $\boldsymbol{x}$ and $\boldsymbol{D}$. From left to right, the columns are optimization results at iteration 0, 15, 50, and 249, respectively. The top row is the result formed by 32 points while the results on the bottom are formed by 98 points.

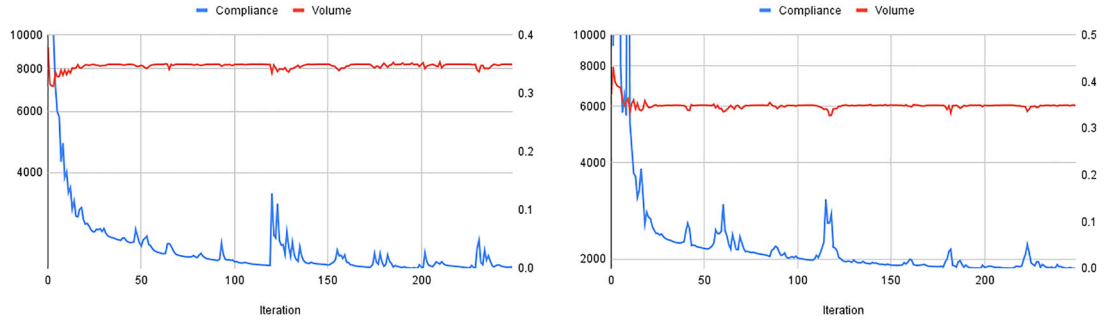

FIGURE 16 Left: The comparison of compliance function curves of cellular structures with free boundary fromed by only optimizing $\boldsymbol{x}$ and optimizing both $\boldsymbol{D}$ and $\boldsymbol{x}$ with 32 Voronoi points. Right: The comparison of compliance function curves of cellular structures with free boundary fromed by only optimizing $\boldsymbol{x}$ and optimizing both $\boldsymbol{D}$ and $\boldsymbol{x}$ with 98 Voronoi points

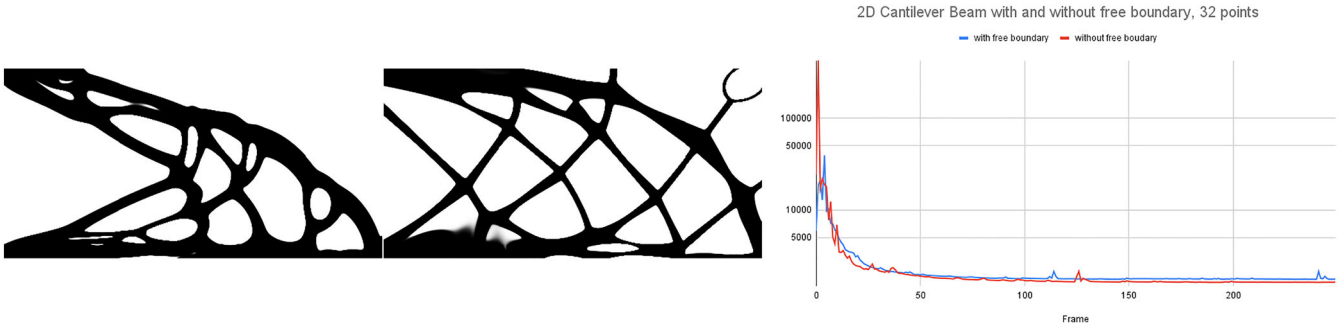

FIGURE 17 Left: The cantilever beam formed with free boundary feature. Middle: The cantilever beam formed without free boundary feature. Right: The comparison of their compliance curves.

5.5 | 3D result and performance

Our method can be easily extended to 3D. Therefore we also demonstrate the 3D cantilever beam in Figure 18. Here, we initialized 128 points inside a $256 \times 128 \times 128$ grid with initial $\boldsymbol{D} = 300I$. Large walls are formed on the bottom and across the top left to the bottom right, connecting nodes receiving force load with the fixed nodes on the left side. We use the isosurface of the optimized density field and render the images in Houdini. We can also add a free boundary for this example in 3D space, as shown in Figure 19. 1024 points are randomly initialized in the grid with initial $\boldsymbol{D} = 700I$. Three-dimensional bubbles are formed and stretched after optimization, and there is no wasted material in the top right corner. Similarly, we compare the resulting in compliance for the optimized 3D cellular structures with and without free boundaries, as shown in Figure 20. For similar reasons, the compliance of the structure with free boundaries is not that much different from that without free boundaries.

The statistics of our high-resolution examples are summarized as in Table 1. These examples are all run on a computer with an Intel i9 9980 CPU, 18 cores, 4GPU NVIDIA GeForce RTX2080, and 128G memory. The convergence criteria given in the table is $|c_i + c_{i-1} - c_{i-2} - c_{i-3}|/(c_{i-2} + c_{i-3}) < 0.1\%$, where i is the iteration number. The forward part includes the time cost of updating the density distribution based on the current variables of the Voronoi structure and the FEM solve for node displacement. The gradient calculation is taking the most time because our algorithm needs to iterate through each cell to calculate the derivative of compliance to each optimizable variable.

5.6 | Discussion

Compared with the standard SIMP method, our topology optimization algorithm with differentiable Voronoi diagrams manifest its computational merits in several aspects. First, the algorithm encodes a strong geometric prior into the optimizer to coerce the emergence of cellular structures, providing a novel design space that was impractical to explore using a conventional density-based method. Second, we propose a free-boundary treatment to overcome the inherent limitation of Voronoi as a domain partition structure. This implicit, free-boundary representation extends our algorithm from

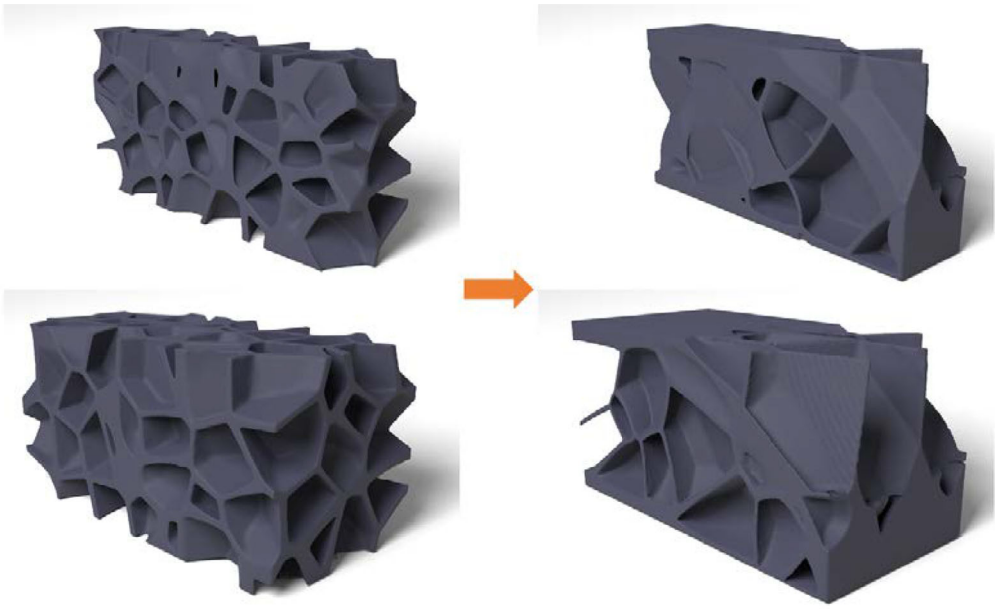

FIGURE 18 Rendered 3D cantilever beam results. Left column is the structure upon initialization, right column is the optimized structure at iteration 150. The top row is the cross-sectional view.

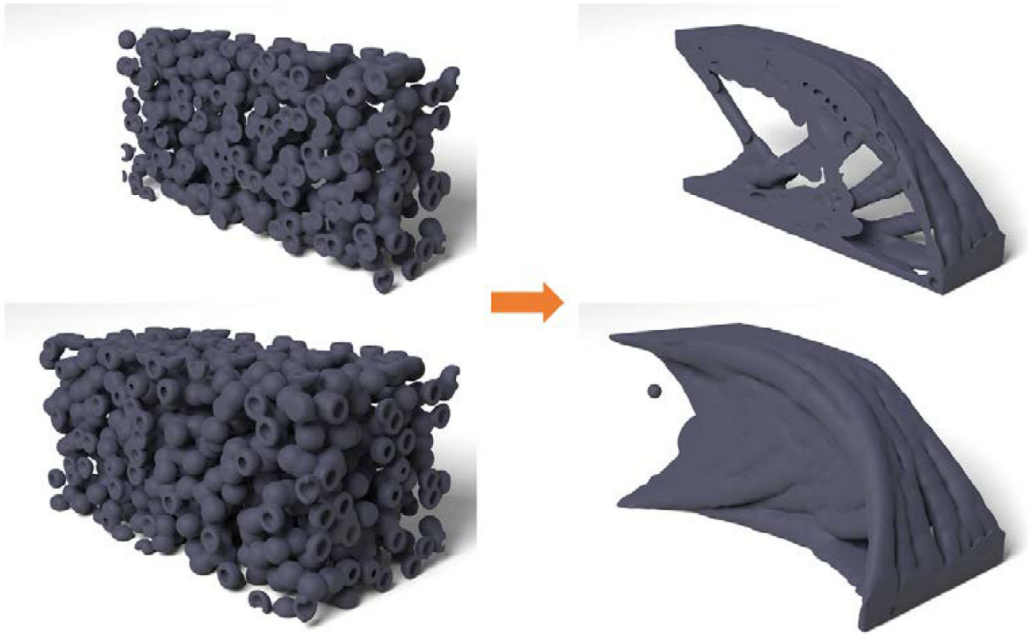

FIGURE 19 Rendered 3D cantilever beam with free boundary results. Left is the structure upon initialization, right is the optimized structure at iteration 100. The top row is the cross-sectional view.

designing the interior part only to handling the optimization of both the boundary shape and the internal structures. Third, the implicit, differentiable nature of our Voronoi diagram provides a practical way to calculate the design sensitivities. Last, regarding the computational performance, the locality of our hybrid grid-particle representation avoids a global search for point neighbors, facilitating large-scale optimizations on a high-resolution FEM grid.

Our approach also manifest several weaknesses compared with the standard SIMP method. First, as shown in the objective curves (e.g., Figure 8C), our approach under-performs in terms of its compliance performance when comparing with SIMP. Because of the additional Voronoi priors employed on top of the density representation, the results tend

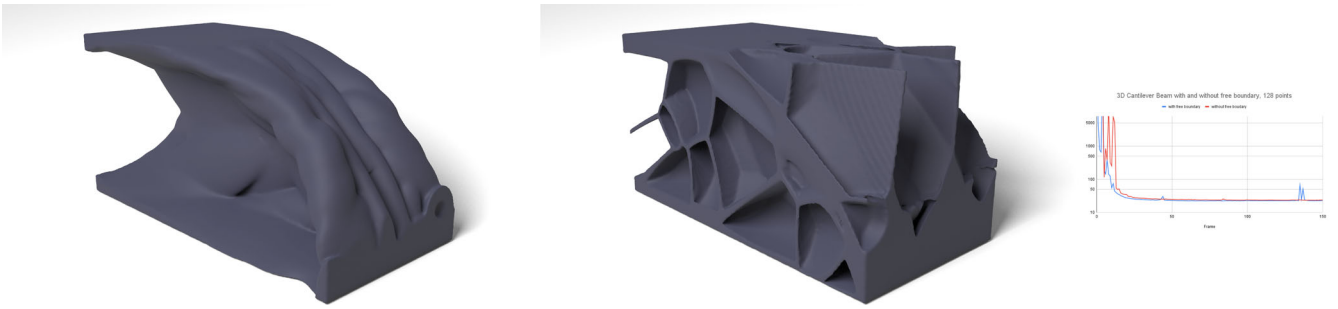

FIGURE 20 Left: The 3D cantilever beam formed with free boundary feature. Middle: The 3D cantilever beam formed without free boundary feature. Right: The comparison of their compliance curves.

TABLE 1 Statistics of high-resolution examples

Example	Resolution	Computation time (s)			Convergence	Neighbor number k
		Forward	Gradient	MMA		
Framed cantilever beam	1024×512	0.721	1.577	0.006	70	10
Odonata wing	1024×256	0.511	1.429	0.004	17	15
Femur bone	1024×1024	1.164	4.915	0.001	49	15
3D cantilever beam	$256 \times 128 \times 128$	2.857	20.18	0.004	39	15
3D cantilever beam with free boundary	$256 \times 128 \times 128$	4.65	80.86	0.021	59	15

to exhibit an ensemble of cellular features of thin membranes and small cells. These features were not favored by a SIMP optimizer, which, in contrast, tend to generate thick beams and large volumes. Second, the free-boundary representation limits the search of structures with optimal compliance too. As shown in Figures 17 and 20, the results with a free-boundary treatment, despite its removal of wasted features in the top-right corner, did not exceed the one without a free boundary (and therefore with wasted features). Third, the computational cost of the implicit Voronoi, in particular the sensitivity $d\rho/d\boldsymbol{x}$, though accelerated by its local search strategy, is highly dependent on the number of neighboring points within the range. A large number of neighboring points, which is necessary to accommodate highly anisotropic cells in some examples (e.g., Figures 13 and 18), leads to a quadratic increase of the computation time for the sensitivity calculation. Devising neighbor-pruning strategies to reduce the soft-max sum calculation for redundant neighbors (i.e., the points not contributing to a cell's density), or devising anisotropic Kd-tree search algorithms, could be an interesting direction to explore.

6 | CONCLUSION

We proposed a topology optimization algorithm for generalized cellular structures. A Voronoi representation that is differentiable, generalized, and encompassing a hybrid discretization is devised to construct an efficient gradient-based optimization framework. The numerical examples demonstrate that the proposed method is effective in generating organic cellular structures resembling those in nature that also minimize structural compliance. Compared to the previous literature in cellular topology optimization, our method enabled, for the first time, a differentiable representation of the previously discrete Voronoi representation and successfully incorporated this representation in a density-based standard topology optimization pipeline. Compared to the previous hybrid Eulerian–Lagrangian topology optimization methods such as References 47, 49, and 45, which relied on an explicit or smoothed Lagrangian representation that can move in an Eulerian domain, our approach encodes the optimization variables into an implicitly defined distance metric tensor field carried on moving particles to express complex cellular structures. The differentiable nature of our geometric representation, in conjunction with its generalized Voronoi cells based on an optimizable, non-Euclidean distance field, allows the optimization of a broad range of organic cellular structures based on first principles.

Still, there are some limitations to our method. First, due to the definition of our differentiable Voronoi representation, the edge formed by two control points is thinner in the middle and thicker farther away from the two points. We anticipate solving this problem by exploring different forms of metric tensors to obtain a controllable and consistent edge thickness over space. Second, the FEM discretization in our method relies on a high-resolution grid on the background, which requires a fine grid discretization to represent a complex structure with many cells. Exploring more efficient Eulerian–Lagrangian representations, in particular, those with sub-cell discretizations, would further reduce the computational cost of the entire optimization pipeline. Third, our current approach handles the free boundary with a fixed ϵ_s value, implying a constant and non-optimizable radius for the foamy boundary. Incorporating ϵ_s into the optimization framework can further enhance the expressiveness of the current model. Fourth, we optimize the wing-shaped structures only in two-dimensional spaces to demonstrate the expressiveness of our proposed differentiable cellular structure. To make a comparison with the Voronoi structures of insect wings in nature, we plan to use our method on shell finite elements. We also consider future work to investigate multi-level cellular structures, featuring cellular structures at multiple length scales with a parent-child relationship, and extend the Voronoi structural representation to other structural optimization problems with different objectives and physical constraints, motivated by the nature of various insect wings that are driven by different biological or mechanical models.

DATA AVAILABILITY STATEMENT

The data that support the findings of this study are available from the corresponding author upon reasonable request.

ORCID

Fan Feng https://orcid.org/0000-0002-4265-1763
Shiying Xiong https://orcid.org/0000-0002-0468-4249
Yuqing Zhou https://orcid.org/0000-0002-1812-068X
Tsuyoshi Nomura https://orcid.org/0000-0002-7055-6675
Bo Zhu https://orcid.org/0000-0002-1392-0928

REFERENCES

1. Qi C, Jiang F, Yang S. Advanced honeycomb designs for improving mechanical properties: a review. *Compos B Eng*. 2021;227:109393.
2. Gautam D, Rao VK. Nondestructive evaluation of mechanical properties of femur bone. *J Nondestruct Eval*. 2021;40(1):1-11.
3. Jongerius S, Lentink D. Structural analysis of a dragonfly wing. *Exp Mech*. 2010;50(9):1323-1334.
4. Kraynik AM. The structure of random foam. *Adv Eng Mater*. 2006;8(9):900-906.
5. Nazir A, Abate KM, Kumar A, Jeng JY. A state-of-the-art review on types, design, optimization, and additive manufacturing of cellular structures. *Int J Adv Manuf Technol*. 2019;104(9):3489-3510.
6. Salcedo MK, Hoffmann J, Donoughe S, Mahadevan L. Computational analysis of size, shape and structure of insect wings. *Biology Open* 2019; 8(10):bio040774.
7. Ma J, Zhao ZL, Lin S, Xie YM. Topology of leaf veins: experimental observation and computational morphogenesis. *J Mech Behav Biomed Mater*. 2021;123:104788.
8. Bousquières J, Michon C, Bonazzi C. Functional properties of cellulose derivatives to tailor a model sponge cake using rheology and cellular structure analysis. *Food Hydrocoll*. 2017;70:304-312.
9. Bock M, Tyagi AK, Kreft JU, Alt W. Generalized Voronoi tessellation as a model of two-dimensional cell tissue dynamics. *Bull Math Biol*. 2010;72(7):1696-1731.
10. Kou X, Tan S. Microstructural modelling of functionally graded materials using stochastic Voronoi diagram and B-spline representations. *Int J Comput Integr Manuf*. 2012;25(2):177-188.
11. Gostick JT. Random pore network modeling of fibrous PEMFC gas diffusion media using Voronoi and Delaunay tessellations. *J Electrochem Soc*. 2013;160(8):F731.
12. Martínez J, Hornus S, Song H, Lefebvre S. Polyhedral Voronoi diagrams for additive manufacturing. *ACM Trans Graph (TOG)*. 2018;37(4):1-15.
13. Lei HY, Li JR, Xu ZJ, Wang QH. Parametric design of Voronoi-based lattice porous structures. *Mater Des*. 2020;191:108607.
14. Voronoi G. Nouvelles applications des paramètres continus à la théorie des formes quadratiques. Deuxième mémoire. Recherches sur les parallélloèdres primitifs. *J für die Reine und Angew Math (Crelles J)*. 1908;1908(134):198-287.
15. Aurenhammer F. Power diagrams: properties, algorithms and applications. *SIAM J Comput*. 1987;16(1):78-96.
16. Springel V. Moving-mesh hydrodynamics with the AREPO code. *Proc Int Astronom Union*. 2010;6(S270):203-206.
17. Ji Z, Fu L, Hu XY, Adams NA. A new multi-resolution parallel framework for SPH. *Comput Methods Appl Mech Eng*. 2019;346:1156-1178.
18. Busto S, Chiocchetti S, Dumbser M, Gaburro E, Peshkov I. High order ADER schemes for continuum mechanics. *Front Phys*. 2020;8:32.
19. Springel V. E pur si muove: Galilean-invariant cosmological hydrodynamical simulations on a moving mesh. *Mon Not R Astron Soc*. 2010;401(2):791-851.

20. Karavelas M. 2D Voronoi diagram adaptor. Vol 5. 4th ed. CGAL Editoral Board; 2022.
21. Ray N, Sokolov D, Lefebvre S, Lévy B. Meshless Voronoi on the GPU. *ACM Trans Graph (TOG)*. 2018;37(6):1-12.
22. Liu X, Ma L, Guo J, Yan DM. Parallel computation of 3D clipped Voronoi diagrams. *IEEE Trans Vis Comput Graph*. 2020;28(2): 1363-1372.
23. Lu L, Sharf A, Zhao H, et al. Build-to-last: strength to weight 3D printed objects. *ACM Trans Graph*. 2014;33(4):1-10.
24. Öncel AC, Yaman U. Generation of optimized Voronoi based interior structures for improved mechanical properties. *Proc Manuf*. 2019;38:42-51.
25. Cucinotta F, Raffaele M, Salmeri F. A stress-based topology optimization method by a Voronoi tessellation additive manufacturing oriented. *Int J Adv Manuf Technol*. 2019;103(5):1965-1975.
26. Hoffmann J, Donoughe S, Li K, Salcedo MK, Rycroft CH. A simple developmental model recapitulates complex insect wing venation patterns. *Proc Natl Acad Sci*. 2018;115(40):9905-9910.
27. Ying J, Lu L, Tian L, Yan X, Chen B. Anisotropic porous structure modeling for 3D printed objects. *Comput Graph*. 2018;70:157-164.
28. Du Q, Faber V, Gunzburger M. Centroidal Voronoi tessellations: applications and algorithms. *SIAM Rev*. 1999;41(4):637-676.
29. Do QT, Nguyen CHP, Choi Y. Homogenization-based optimum design of additively manufactured Voronoi cellular structures. *Addit Manuf*. 2021;45:102057.
30. Wu J, Aage N, Westermann R, Sigmund O. Infill optimization for additive manufacturing—Approaching bone-like porous structures. *IEEE Trans Vis Comput Graph*. 2017;24(2):1127-1140.
31. Yi B, Zhou Y, Yoon GH, Saitou K. Topology optimization of functionally-graded lattice structures with buckling constraints. *Comput Methods Appl Mech Eng*. 2019;354:593-619.
32. Schmidt MP, Pedersen CB, Gout C. On structural topology optimization using graded porosity control. *Struct Multidiscip Optim*. 2019;60(4):1437-1453.
33. Martínez J, Dumas J, Lefebvre S. Procedural Voronoi foams for additive manufacturing. *ACM Trans Graph (TOG)*. 2016;35(4):1-12.
34. Tian L, Lu L, Chen W, Xia Y, Wang CC, Wang W. Organic open-cell porous structure modeling. Symposium on Computational Fabrication; 2020:1-12.
35. Bendsoe MP, Sigmund O. *Topology Optimization: Theory, Methods, and Applications*. Springer Science & Business Media; 2003.
36. Wu J, Dick C, Westermann R. A system for high-resolution topology optimization. *IEEE Trans Vis Comput Graph*. 2015;22(3):1195-1208.
37. Liu H, Hu Y, Zhu B, Matusik W, Sifakis E. Narrow-band topology optimization on a sparsely populated grid. *ACM Trans Graph (TOG)*. 2018;37(6):1-14.
38. Wu J, Wang W, Gao X. Design and optimization of conforming lattice structures. *IEEE Trans Vis Comput Graph*. 2019;27(1):43-56.
39. Groen JP, Stutz FC, Aage N, Bærentzen JA, Sigmund O. De-homogenization of optimal multi-scale 3D topologies. *Comput Methods Appl Mech Eng*. 2020;364:112979.
40. Telgen B, Sigmund O, Kochmann D. Topology optimization of graded truss lattices based on on-the-fly homogenization. *J Appl Mech*. 2022;86:1-40.
41. Zhou Y, Lohan DJ, Zhou F, Nomura T, Dede EM. Inverse design of microreactor flow fields through anisotropic porous media optimization and dehomogenization. *Chem Eng J*. 2022;435:134587.
42. Zhu B, Skouras M, Chen D, Matusik W. Two-scale topology optimization with microstructures. *ACM Trans Graph (TOG)*. 2017;36(4):1.
43. Deng J, Chen W. Concurrent topology optimization of multiscale structures with multiple porous materials under random field loading uncertainty. *Struct Multidiscip Optim*. 2017;56(1):1-19.
44. Wang Y, Kang Z. Concurrent two-scale topological design of multiple unit cells and structure using combined velocity field level set and density model. *Comput Methods Appl Mech Eng*. 2019;347:340-364.
45. Li Y, Li X, Li M, Zhu Y, Zhu B, Jiang C. Lagrangian–Eulerian multidensity topology optimization with the material point method. *Int J Numer Methods Eng*. 2021;122(14):3400-3424.
46. Cho S, Kwak J. Topology design optimization of geometrically non-linear structures using meshfree method. *Comput Methods Appl Mech Eng*. 2006;195(44-47):5909-5925.
47. Guo X, Zhang W, Zhong W. Doing topology optimization explicitly and geometrically—A new moving morphable components based framework. *J Appl Mech*. 2014;81(8):JAM-14-1162.
48. Liu C, Du Z, Zhang W, Zhu Y, Guo X. Additive manufacturing-oriented design of graded lattice structures through explicit topology optimization. *J Appl Mech*. 2017;84(8):JAM-17-1271.
49. Norato J, Bell B, Tortorelli DA. A geometry projection method for continuum-based topology optimization with discrete elements. *Comput Methods Appl Mech Eng*. 2015;293:306-327.
50. Kazemi H, Vaziri A, Norato JA. Multi-material topology optimization of lattice structures using geometry projection. *Comput Methods Appl Mech Eng*. 2020;363:112895.
51. Williams F, Parent-Levesque J, Nowrouzezahrai D, Panozzo D, Yi KM, Tagliasacchi A. Voronoinet: general functional approximators with local support. Proceedings of the IEEE/CVF Conference on Computer Vision and Pattern Recognition Workshops; 2020:264-265.
52. Richter R, Alexa M. Mahalanobis centroidal Voronoi tessellations. *Comput Graph*. 2015;46:48-54.
53. Shamos MI, Hoey D. Closest-point problems. Proceedings of the 16th Annual Symposium on Foundations of Computer Science; 1975:151-162.
54. Boltzmann L. Studien uber das Gleichgewicht der lebenden Kraft. *Wissenschafiliche Abhandlungen*. 1868;1:49-96.
55. Bridle JS. Probabilistic interpretation of feedforward classification network outputs, with relationships to statistical pattern recognition; 1990:227-236.

56. Mahalanobis PC. On the generalized distance in statistics; 1936; National Institute of Science of India.
57. Ferrari F, Sigmund O. A new generation 99 line Matlab code for compliance topology optimization and its extension to 3D. *Struct Multidiscip Optim*. 2020;62(4):2211-2228.
58. Wang F, Lazarov BS, Sigmund O. On projection methods, convergence and robust formulations in topology optimization. *Struct Multidiscip Optim*. 2011;43(6):767-784.
59. Sigmund O. A 99 line topology optimization code written in Matlab. *Struct Multidiscip Optim*. 2001;21(2):120-127.
60. Liu K, Tovar A. An efficient 3D topology optimization code written in Matlab. *Struct Multidiscip Optim*. 2014;50(6):1175-1196.
61. Svanberg K. The method of moving asymptotes—a new method for structural optimization. *Int J Numer Methods Eng*. 1987;24:359-373.
62. Dumas J. mma; 2018. https://github.com/jdumas/mma
63. Sethian JA. Fast marching methods. *SIAM Rev*. 1999;41(2):199-235.

How to cite this article: Feng F, Xiong S, Liu Z, et al. Cellular topology optimization on differentiable Voronoi diagrams. *Int J Numer Methods Eng*. 2022;1-23. doi: 10.1002/nme.7121